Arctic Science

OPEN ACCESS | Research Article

High-resolution mapping of snow depth and snow thermal insulation using low-cost UAVs in complex Arctic Urban Terrains

Marlin M. Mueller[a], **Steffen Dietenberger**[a], **Clémence Dubois**[a], **Soraya Kaiser**[b], **Pauline Walz**[c], **Josefine Lenz**[b], **Oliver Fritz**[c], **Sabrina Marx**[c], **Christian Thiel**[a], **and Moritz Langer**[b,d]

[a]Institute of Data Science, German Aerospace Center (DLR), Mälzerstraße 3-5, 07745 Jena, Germany; [b]Permafrost Research Section, Alfred Wegener Institute (AWI), Helmholtz Centre for Polar and Marine Research, Telegrafenberg A45, 14473 Potsdam, Germany; [c]Heidelberg Institute for Geoinformation Technology (HeiGIT), Schloss-Wolfsbrunnenweg 33, 69118 Heidelberg, Germany; [d]Department of Earth Sciences, Vrije Universiteit Amsterdam, De Boelelaan 1085, 1081 HV Amsterdam, the Netherlands

Corresponding author: **Marlin M. Mueller** (email: marlin.mueller@dlr.de)

Abstract

Arctic communities on permafrost face infrastructure instability from climate-driven thawing, a process exacerbated by the insulating effect of snow accumulation around buildings and roads. To monitor this threat, we assess the feasibility of using a low-cost, consumer-grade unoccupied aerial vehicle (UAV) (DJI Mini 2) with Structure-from-Motion photogrammetry to map snow depth and derive thermal insulation metrics in Aklavik, NT, Canada. By differencing high-resolution snow-covered (March 2024) and snow-free (September 2022) datasets, we found a mean snow depth of 0.65 m across the 0.98 km^2 study area. Critically, snow was deeper adjacent to roads (mean: 0.65 m) than buildings (0.59 m), creating stronger thermal insulation along transportation corridors. This translated into a substantial warming bias ($\Delta T_s > 2.0$ °C) for over 45% of road-adjacent and 35% of building-adjacent areas. Validation revealed a slight overestimation on bare ground (+8.24 cm) but a systematic underestimation relative to probe measurements (bias: −17.32 cm), primarily because the snow-free survey captured the top of shrub canopies rather than the true ground surface. This study demonstrates that carefully processed data from accessible UAV technology can provide valuable, high-resolution insights into hazardous snow distribution, offering a cost-effective and scalable tool to support permafrost stability and infrastructure management.

Key words: UAV, snow depth, permafrost, Structure-from-Motion, Arctic infrastructure, community-based monitoring

1. Introduction

In the Arctic, permafrost is an essential factor for the ecosystem and serves as the fundamental load-bearing substrate upon which human settlements and infrastructure are built (Manos et al. 2025). However, the Arctic is warming at a rate almost four times faster than the global average (Rantanen et al. 2022), leading to widespread permafrost degradation (Nitzbon et al. 2024). This thaw compromises the structural integrity of the ground, resulting in substantial stability challenges for Arctic infrastructure (Schneider von Deimling et al. 2021). Observed impacts include loss of bearing capacity for building foundations and differential settlement or ground subsidence affecting roads, pipelines, and airstrips, incurring substantial economic costs projected to escalate in the coming decades (Hjort et al. 2022; Streletskiy et al. 2023; Manos et al. 2025). Assessing and mitigating these risks requires accurate monitoring and understanding of the processes governing permafrost thermal regimes.

Snow cover plays a critical role in modulating the thermal state of permafrost (Stieglitz et al. 2003; Park et al. 2015; Damseaux et al. 2025). There is a positive relationship between snow depth and ground temperatures, as the insulating properties of snow inhibit heat loss from the ground during winter (Johansson et al. 2013; Khani et al. 2022). Additionally, in areas with high snow accumulation, snow melt can lead to ponding surface water, further increasing heat uptake during the melting season (Hinkel and Hurd Jr. 2006). Variations in snow cover duration (SCD) and snow depth directly influence active layer thickness and overall permafrost stability (Ling and Zhang 2003). Snow distribution is highly heterogeneous, particularly in inhabited areas where wind redistribution results in pronounced drift accumulation and erosion patterns around natural topography and anthropogenic structures such as buildings and roads (Schneider von Deimling et al. 2021; Chen et al. 2023; Aga et al. 2025). Deep snowdrifts adjacent to infrastructure can enhance localized ground insulation, potentially accelerating thaw beneath or adjacent to foundations and embankments, thereby exacerbating infrastructure stability problems (Aga et al. 2025). This issue is amplified through human snow management, where

snow is piled up next to roads and buildings to clear roads and driveways (O'Neill and Burn 2017; Hjort et al. 2022). Monitoring this fine-scale variability in snow depth is therefore crucial for understanding localized permafrost thaw hazards (Aga et al. 2025).

However, established measurement methods generally fail to provide the necessary spatial resolution at comparable costs or effort. Traditional manual probing (Prokop et al. 2008) is labor-intensive, provides only sparse point measurements, and can be inaccurate due to over-probing into soft soil or under-probing on ice layers. Furthermore, probing can be hazardous in remote or complex terrain and may disturb the snowpack, influencing subsequent measurements (Deems et al. 2013). Terrestrial remote sensing techniques like Laser Scanning or Ground-Penetrating Radar are often hampered by logistical challenges and line-of-sight occlusions in complex terrain (Eker et al. 2019; Vergnano et al. 2022). Furthermore, airborne methods such as LiDAR or large-format photogrammetry (Deems et al. 2013; Bühler et al. 2015), while capable of high-resolution mapping, remain prohibitively expensive and weather-constrained for frequent monitoring by local communities. Conversely, available satellite-based products and model estimations, such as the 24 km resolution data from the Canadian Meteorological Centre (CMC) (Brown and Brasnett 2010; Luojus et al. 2021), provide data at resolutions far too coarse to resolve the fine-scale snow variability around infrastructure.

The emergence of low-cost unoccupied aerial vehicles (UAVs) coupled with Structure from Motion (SfM) photogrammetry presents a paradigm shift for local fine-scale snow depth monitoring (Cimoli et al. 2017; Gaffey and Bhardwaj 2020; Jacobs et al. 2021). By differencing snow-covered and snow-free digital surface models (DSMs) (Gabrlik et al. 2019), high-resolution, spatially continuous snow depth maps suitable for analyzing infrastructure-scale variability can be generated (Van der Sluijs et al. 2018; Lendzioch et al. 2019). Previous studies using professional-grade UAVs in alpine, glacier, and tundra environments have achieved vertical accuracies (root mean square error, RMSE) typically ranging from 8 to 40 cm (Bernard et al. 2021; Masný et al. 2021; Maier et al. 2022; Meriö et al. 2023). However, the accuracy of the snow-free reference DSM remains critical; dense vegetation, such as shrubs, can obscure the true ground surface, leading to systematic underestimation of snow depth (Vander Jagt et al. 2015; Harder et al. 2020; Lamare et al. 2023). Conversely, snow depth can be overestimated if tall vegetation protrudes through the winter snowpack. While photogrammetry has been validated in natural tundra environments using professional systems (Walker et al. 2020), the potential of consumer-grade hardware to achieve comparable results in complex terrain remains a key area of investigation.

Deploying UAVs in Arctic communities introduces specific challenges distinct from natural landscapes, including complex obstacles and harsh operating conditions. While professional fixed-wing systems offer superior coverage, lightweight consumer-grade multirotors significantly reduce regulatory and financial barriers for community-based deployment (Pina and Vieira 2022). However, reliability in these environments depends heavily on factors such as optimal illumination (Revuelto et al. 2021) and accuracy near vertical structures (Clark et al. 2018, 2023). To the authors' knowledge, no published studies have specifically employed low-cost UAVs within Arctic communities to monitor fine-scale snow distribution or linked such datasets to a quantitative analysis of snow insulation patterns relevant to permafrost and infrastructure stability.

A critical requirement for accurate change detection using multitemporal UAV datasets is the precise co-registration of point clouds or DSMs. While the use of accurately surveyed Ground Control Points (GCPs) is the standard approach to improve georeferencing (Nota et al. 2022), the requirement for additional survey-grade equipment and survey execution creates a substantial logistical and financial barrier for community-led initiatives aiming for minimal operational complexity. To reduce reliance on concurrent field surveys, complementary strategies combine novel flight designs Mueller et al. (2023) with advanced alignment algorithms, such as the iterative closest point (ICP) method (Kaiser et al. 2022) or image co-alignment (Nota et al. 2022). These techniques improve relative accuracy computationally, effectively shifting the complexity from the field (removing the need for RTK equipment) to postprocessing, which presents a beneficial trade-off for nonexpert monitoring programs.

This research is situated within the "UndercoverEisAgent en" project, which collaborates with a secondary school and community members in the Canadian Arctic (Fritz et al. 2022; Mueller et al. 2024). We aim to assess the capabilities of very low-cost, consumer-grade UAV technology, specifically the DJI Mini 2, for high-resolution monitoring of snow depth spatial variability around buildings and road networks within the Arctic community of Aklavik, NT, Canada (Fig. 1). The potential benefits include cost reductions, the ability to safely survey inaccessible areas on-demand, and the generation of data at spatial resolutions pertinent to infrastructure-scale processes (Manos et al. 2025). Consequently, the focus of this work is not to maximize geodetic precision for its own sake, but to assess the feasibility of a workflow where community members can provide the necessary data to derive actionable risk maps of potential warming hotspots due to snow accumulation. This shift towards accessibility aims to facilitate future self-sufficient monitoring campaigns relevant to local infrastructure and climate adaptation planning. It is important to note that the subsequent thermal analysis represents a first-order assessment of warming potential based on simplified steady-state assumptions, intended to highlight relative risk patterns rather than quantify absolute ground thermal regimes.

2. Study area

The Mackenzie Delta region is recognized as one of the most rapidly changing permafrost landscapes globally, attributed to its ice-rich terrain, rapid erosion and sedimentation driven by fluvial processes, and substantial climate warming, including an approximate 2.5 °C increase in mean annual air temperature since 1970 (Burn and Kokelj 2009). More locally, our analysis of data from the Aklavik weather

Fig. 1. Overview of the study area in Aklavik, NT, Canada. (*a*) The top-left inset map shows the location of Aklavik within Canada. (*b*) Snow-free unoccupied aerial vehicle (UAV) orthomosaic of Aklavik acquired on 21 September 2022. (*c*) Snow-covered UAV orthomosaic of Aklavik acquired on 24 March 2024, with overlaid in situ snow depth measurements. The legend in panel (*c*) indicates in situ measured snow depth categories in centimeters (cm). Background imagery for orthomosaics from Google Maps (Google 2025).

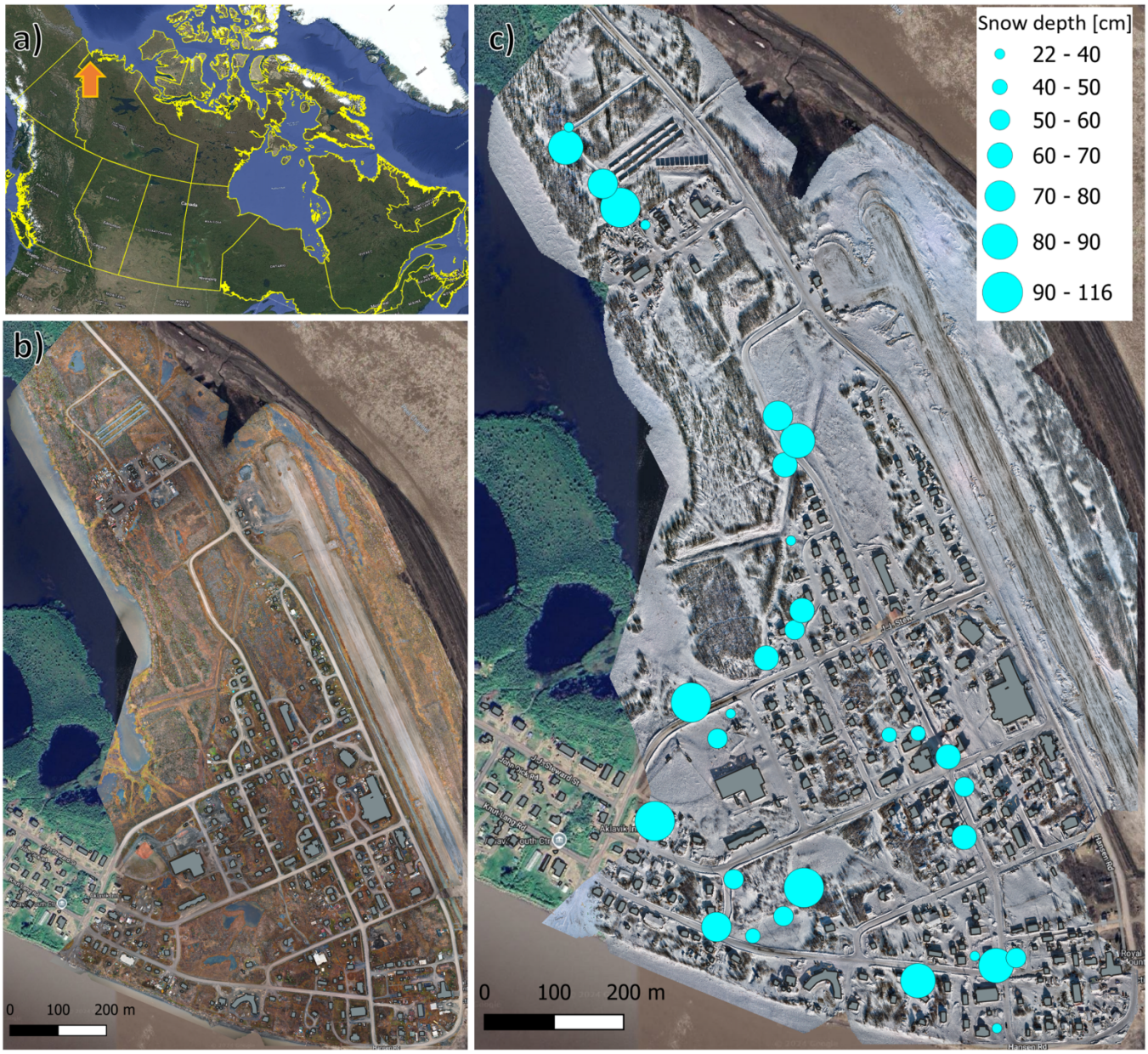

station indicates a mean annual temperature trendline of +1.23 °C per decade for the period 1982–2009 (period selected due to data gaps) (Government of Canada 2024). During the recent study period (2021–2024), the overall mean temperature recorded was −6.65 °C; the mean Arctic summer temperature (June–September) was 11.81 °C, and the mean Arctic winter temperature (October–May) was −15.95 °C (Government of Canada 2024).This observed warming trend in Aklavik is consistent with the substantial climate shifts documented across the broader Mackenzie River Delta (Gill et al. 2014; Van der Sluijs et al. 2018). Model-derived snow depth estimates for Aklavik (2010–2020), based on the 24 km resolution CMC Daily Snow Depth Analysis Data and assessed for March, ranged from 0.3 to 0.6 m, with a median of 0.43 m (Brown and Brasnett 2010). Looking ahead, climate projections suggest complex shifts in Arctic snow dynamics, with increased winter precipitation potentially offsetting shorter snow cover duration (Callaghan et al. 2012). By the end of the century, snow cover is projected to start about 2 weeks later in autumn and end about 2 weeks earlier in spring (Mohammadzadeh Khani et al. 2022; Derksen and Mudryk 2023). Given these uncertainties, high-resolution monitoring

is essential to capture the actual local snow conditions affecting infrastructure.

The hamlet of Aklavik is located on the banks of the Peel channel, a distributary of the Peel river in the Mackenzie river delta in the NT, Canada (Fig. 1*a*). It stretches around 1.8 km in east–west direction and 1.4 km in north–south direction. Aklavik's population is estimated at 644 residents as of 1 July 2024 (NWT Bureau of Statistics 2024). The village consists of roughly 350 buildings ranging from small sheds to a few multistory large commercial or governmental buildings like the Moose Kerr school, the main administrative building, and two supermarkets. The majority of buildings are free standing single family homes built on pilings creating space between the foundation and the underlying soil. However, thawing of this permafrost can compromise such foundations by reducing their bearing capacity and causing differential settlement, which poses severe risks to the structural integrity of these homes (Hjort et al. 2022; Manos et al. 2025). The roads and pathways within the community are comprised of compacted soil and gravel which also includes the local airstrip. Vegetation throughout Aklavik is dominated by grasses and shrubs with smaller interspersed groves of deciduous birch and alder reaching only a few meters in height. While the westward Northern Richardson Mountains range is characterized by ice-rich permafrost, the delta itself is largely characterized by extensive discontinuous permafrost with medium to low ice content (Natural Resources Canada 2023). Snow is actively managed in the community through the regular clearing of roads and driveways, a process that typically results in snow being piled up along the sides of these infrastructure elements and around buildings.

3. Materials and methods

3.1. Remote sensing data

The UAV platform used was a DJI Mini 2, a commercially available consumer-grade drone, with a cost of roughly $350 per unit. It is equipped with a 12-megapixel camera system capable of capturing high-resolution images in raw DNG format and utilizes a standard Global Navigation Satellite System (GNSS) receiver (supporting GPS, GLONASS, and Galileo) for image geotagging, which has a nominal positional accuracy of ±1.5 m horizontally and ±0.5 m vertically (aided by barometric altimetry) (DJI 2021). For a comprehensive list of the DJI Mini 2's technical specifications, please refer to Table 1.

The UAV survey employed a novel flight pattern, in which the drone starts its flight over a defined reference point at 120 m above ground level (AGL) and then flies outward in a spiral trajectory (Mueller et al. 2023). This flight pattern was chosen to optimize the geometric accuracy of the resulting DSM, particularly in areas with subtle topographic variations, which are common in permafrost landscapes. To cover the entire study area, a mosaic of these spiral sub-missions was flown. Unlike standard nadir surveys, this flight pattern continuously varies the camera gimbal angle (pitch) from 0° to 35° off-nadir. This resulted in variable capture angles that combine the advantages of both nadir and oblique data acquisition methods described in detail in Mueller et al. (2023).

Two UAV surveys were conducted over Aklavik to acquire high-resolution imagery: a snow-free "summer" survey in September 2022 and a snow-covered "winter" survey in March 2024. Table 2 provides detailed information on the specific acquisition parameters for each survey, including flight details, imagery specifications, and equipment used. All acquired datasets were subsequently resampled to a common resolution of 5 cm/pixel.

It is important to note that during the September 2022 survey, two flight missions connecting the western edge and central parts of Aklavik encountered unusually high vertical GNSS errors exceeding 60 m. These errors were largely nonsystematic and could not be rectified through standard postprocessing methods, such as applying simple offsets or utilizing homologous point matching techniques. This issue led to significant nonsystematic vertical errors in the resulting DSM for the affected areas, making the creation of an accurate difference dataset impossible for that portion. Consequently, the western part of Aklavik was omitted from this study, resulting in a final study area size of 0.98 km^2 (0.864 km^2 excluding no data values). Comparisons and statistics were restricted exclusively to this overlapping extent to ensure consistency between the seasonal datasets.

The imagery was processed using Agisoft Metashape (version 1.8.4 for the 2022 data, and version 2.1.3 for the 2024 data), generating sparse and dense point clouds, DSMs, and orthomosaics (see Appendix A1). The inaccurate absolute GNSS altitude in the image metadata was replaced by combining the drone's precise relative barometric altitude with the known ground elevation of the takeoff point (Mueller et al. 2023), derived from the local 2 m resolution ArcticDEM (Porter et al. 2022). The aligned UAV-derived datasets in 10 cm/pixel resolution are openly available (Mueller et al. 2025). Processing for both datasets was performed on a local workstation featuring 128 GB RAM, an Intel©Xeon©CPU E5-2640 v4 @ 2.40 GHz processor, and dual GPUs (Nvidia Quadro P4000 and Quadro P5000).

3.2. In situ snow depth measurements

In situ snow depth measurements were conducted throughout Aklavik to provide validation data for snow depth estimations derived from the UAV-based remote sensing data presented in this study. Snow depth was manually quantified using a graduated metal probe, a standard technique for point-based snow depth assessment (Prokop et al. 2008). The probe, marked at 5 cm intervals, allowed for rapid and direct measurement of snow depth with a precision of ±5 cm. A total of 44 measurement sites were selected across the study area, prioritizing locations with undisturbed snow cover to minimize the influence of anthropogenic compaction or redistribution. At each site, five individual snow depth measurements were taken with the probe within a 2 m radius of a designated central point. This approach provides a localized average snow depth and captures small-scale variability. The geographic coordinates of each central measurement point were initially recorded using the integrated GNSS receiver of a Samsung Galaxy A52s smartphone. Due to the inherent

Table 1. UAV specifications of DJI Mini 2.

UAV specification	DJI Mini 2
GNSS	GPS/GLONASS/Galileo
Image sensor	DJI FC7303; 1/2.3″-CMOS; focal length 24 mm (35 mm equivalent)
Max. wind resistance	10.8 m/s
No. of pixels	4000 × 3000 (12 MP)
Focal length	4.49 mm
Field of view	73° (horizontal); 53° (vertical); 84° (diagonal)
Electronic shutter	4-1/8000 s
Data format	DNG (16-bit)
Aircraft weight	249 g

Note: GNSS, Global Navigation Satellite System; UAV, unoccupied aerial vehicle.

Table 2. UAV survey acquisition parameters.

Parameter	September 2022 survey ("summer")	March 2024 survey ("winter")
Survey date	2022-09-21	2024-03-24
Number of flight missions	19	13
Number of images captured	5157	3532
Images per sub-mission	271	272
Total mission flight time	5 h 23 min	3 h 41 min
Image format	DNG (16 bit)	
Nominal flight altitude (AGL)	124 m	118 m
Average ground resolution	4.65 cm/pixel	4.40 cm/pixel
Survey area coverage	2.85 km^2	1.47 km^2
UAV model	DJI Mini 2	
Camera model	FC7303	
Control application	Litchi (Version 4.25.0)	Litchi (Version 4.26.6)
Flight pattern	Pre-programmed spiral waypoints	
Camera acquisition parameters	Auto	

Note: AGL, above ground level; UAV, unoccupied aerial vehicle.

limitations of smartphone GNSS, positional accuracy was limited to a few meters.

To improve the spatial accuracy of the snow depth measurements, the recorded locations were subsequently refined through manual co-registration with the high-resolution UAV-derived orthomosaic. This alignment was facilitated by the visible foot tracks left in the snow during the measurement process, which were clearly discernible in the orthomosaic imagery. This manual alignment procedure substantially improved the spatial correspondence between the in situ measurements and the UAV dataset, enabling more robust validation. The spatial distribution of the measurement sites, ranging from snow depths between 0.16 and 1.16 m, is shown in Fig. 1.

3.3. Snow depth map generation and accuracy assessment

3.3.1. Point cloud alignment and offset correction

To minimize the initial offset between the September 2022 reference and March 2024 point clouds, a fine registration step was performed using the ICP algorithm implemented in CloudCompare (version 2.13.2, "Kharkiv"). The ICP algorithm iteratively refines the alignment between two point clouds by minimizing the distance between corresponding points. Prior to alignment, significant offsets were observed between the point clouds, as exemplified by the sample X, Y, and Z differences in Fig. 3.

The CloudCompare implementation utilizes a modified ICP algorithm, based on the work of Zinßer et al. (2005), which integrates scale estimation alongside rotation and translation. One point cloud is designated as the "Reference" (fixed), and the other as the "Data" (to be transformed). The algorithm proceeds iteratively: first, corresponding points are found between the two clouds. Then, a transformation (rotation matrix, translation vector, and optionally a scale factor) is computed that minimizes the root mean square (RMS) distance between corresponding points. This transformation is then applied to the "Data" cloud. The process repeats until convergence, defined by the change in RMSE between iterations falling below a specified threshold (see Appendix A2). This process effectively registers the point clouds even when one depicts snow-covered conditions and the other snow-free con-

Fig. 2. Workflow diagram illustrating the data processing steps for UAV-based snow depth map generation and validation. The main pipeline involves: (1) ICP alignment of the 2022 (snow-free reference) and 2024 (snow-on) point clouds; (2) calculation of an initial difference dataset from the aligned data; (3) creation of a "Distortion Map" by extracting values from the difference dataset at "no difference" elevation points and applying Ordinary Kriging; and (4) generation of a "Corrected Elevation Difference Map" (final snow depth map) using the Distortion Map. A parallel process shows the preparation of in situ snow depth measurements for a combined validation analysis. ICP, iterative closest point; UAV, unoccupied aerial vehicle.

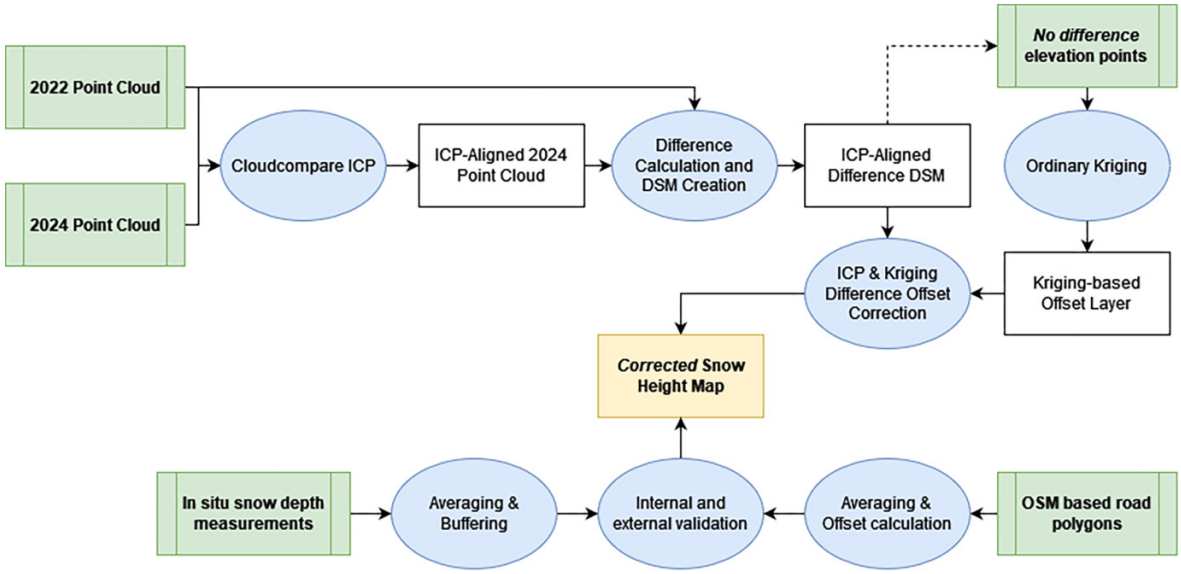

ditions, by aligning stable, corresponding features (e.g. buildings) present in both. A more detailed description of the importance of accurate point cloud alignment was described in Kaiser et al. (2022) also using consumer-grade UAV hardware. Subsequently, the registered September 2022 (reference) and March 2024 (aligned) point clouds were rasterized to generate their respective DSMs, which were then exported as GeoTIFFs with a 5 cm/pixel. Subsequently, residual vertical offsets between the September 2022 and March 2024 DSMs were addressed. A difference raster was calculated by subtracting the March 2024 DSM from the September 2022 DSM (March 2024 to September 2022) (see Fig. 2). This difference raster revealed systematic biases that, while reduced by the ICP alignment, remained present.

To quantify and correct these residual offsets, 205 sampling points were manually selected across the study area, targeting locations where no true elevation change was expected between the two acquisition dates. These locations included snow-free rooftops, cleared and snow-free roads, and the airport runway. The elevation difference at each of these points was extracted from the difference raster, providing a sparse dataset of residual vertical offsets. True GCPs with RTK-GNSS accuracy were not available. It is also important to note that commercially and openly available satellite imagery and map layers, e.g., Google Maps, Bing Maps, OpenStreetMaps (OSM), show horizontal offsets in the range of multiple meters and cannot be used as an absolute reference at the location of the study area (Google 2025; Microsoft 2025; OpenStreetMap contributors 2025).

Ordinary Kriging, a geostatistical interpolation technique, was used to generate a continuous residual offset map or "distortion map" from the sparse offset data. This map represents the estimated systematic vertical error across the entire study area. The Kriging was performed using the "pykrige" library in Python (version 3.12.8). A spherical variogram model was selected, reflecting the expected spatial correlation of the residual offsets. A 2000 × 2000 grid was created, spanning the extent of the study area, to serve as the interpolation grid. The Kriging algorithm estimated the elevation difference and the associated variance at each grid point. The resulting interpolated surface, representing the estimated residual offset was then exported as a GeoTIFF. Finally, this "residual offset map" was subtracted from the March 2024 DSM, effectively correcting the spatially varying systematic bias. This process resulted in a refined March 2024 DSM that is more accurately aligned to the September 2022 reference DSM, representing a "best" relative fit achieved by minimizing discrepancies on assumed stable, snow-free surfaces common to both datasets. Consequently, the subsequent differencing of these aligned DSMs is intended to yield snow depth measurements with minimal systematic bias.

3.3.2. Validation with in situ measurements

The snow depth estimation map is derived by subtracting the reference DSM from the previously aligned DSM of March 2024. The remaining difference should only contain the elevation difference caused by snow accumulation, as vegetation or man-made objects should not have changed substantially between autumn of 2022 and spring of 2024. To evaluate the accuracy of the UAV-derived snow depth estimations, a comparison with the in situ snow depth measurements was conducted. A 2 m buffer was created around each corrected in situ measurement location using QGIS (version 3.34.12,

"Prizren"). Within each buffer, summary statistics, including the mean, median, and standard deviation of the extracted pixel values, were calculated.

The analysis was designed to compare the median UAV-derived snow depth within a 2 m buffer around each in situ point using metrics such as the coefficient of determination (R^2), bias, and RMSE. A known potential limitation of this method is the influence of vegetation on SfM-derived surface models. In situ probes measure depth to the true ground, whereas the UAV method determines snow depth relative to a snow-free surface model that may capture the top of the vegetation canopy instead of the ground itself. To account for this potential source of error and to provide an independent accuracy assessment on bare surfaces, a qualitative visual analysis of land cover was included, and a supplementary validation using snow-cleared roads was performed.

3.3.3. Validation with snow-cleared roads

Due to the limitations of the in situ snow depth comparison, particularly in areas with vegetation, a supplementary internal validation approach was implemented. This method leveraged the assumption that snow-cleared roads should exhibit a near-zero elevation difference between the September 2022 (snow-free) and March 2024 (snow-covered, but roads cleared) DSMs. This approach provides an independent assessment of the systematic error in the elevation difference map, separate from the complexities introduced by vegetation cover.

Road centerlines throughout Aklavik were extracted from the OSM street dataset. A 1 m buffer was generated around these road centerlines in QGIS, creating polygons representing the center two meters of the cleared road surfaces. In person observations confirmed that these road segments were indeed cleared of snow down to the bare road surface during the March 2024 survey. For each buffered road polygon, the same statistical analysis as applied to the in situ measurement locations was performed. The mean, median, and standard deviation values for all road segments were extracted from the September 2022 to March 2024 elevation difference raster. Under ideal conditions, we expect an elevation difference along these cleared roads of 0 cm. In reality, deviations represent a composite of systematic map bias and physical surface changes (e.g., erosion or heave). However, the median offset across the network minimizes these localized physical anomalies, providing a robust estimate of the systematic alignment error.

3.4. Infrastructure mapping

To identify and delineate building footprints within the study area, a semi-automated approach leveraging the DSM was employed. This process utilized the watershed segmentation algorithm implemented in the Orfeo ToolBox (OTB, version 8.1.2) within the QGIS environment (Li et al. 2010). For this process, the March 2024 DSM was inverted so that building roofs represented topographic local minima. The algorithm identifies these "catchment basins" and delineates their footprints by simulating the flooding of the inverted surface until the steep gradients of the building walls are encountered. Key parameters were selected to optimize building extraction, see Appendix A3. The segmentation process generated a shapefile containing polygons representing potential building footprints. To refine the results, a two-step post-processing procedure was applied. First, a size-based filtering was performed, removing polygons with areas smaller than 15 m^2 and larger than 4000 m^2. These thresholds were chosen empirically to exclude very small objects (likely not buildings) and very large polygons (likely encompassing non-building areas). Second, the remaining polygons were simplified using a distance-based simplification algorithm (Tolerance value: 1 m) (Douglas and Peucker 1973), reducing the number of vertices in the polygon geometries while preserving their overall shape.

To provide an independent assessment of the accuracy of the semi-automatically extracted building footprints, a comparison with OSM (OpenStreetMap contributors 2025) building data was performed. OSM data, while not representing a definitive ground truth, offer a readily available reference dataset for building locations. The OSM building data for the Aklavik region were downloaded and due to the known positional inaccuracies of OSM data in this area (see Section 3.3.1), a manual systematic (X and Y shift) alignment of the OSM building shapefile to the March 2024 orthomosaic was performed. This alignment aimed to minimize the positional discrepancies between the two datasets. Following alignment, standard metrics for assessing object detection performance were calculated: Intersection over Union (IoU), precision, recall, and F1 score. These metrics quantify the overlap and area agreement between the extracted building polygons and the OSM building polygons:

$$\text{IoU} = \frac{|A \cap B|}{|A \cup B|} \quad (1)$$

$$\text{Precision} = \frac{\text{TP}}{\text{TP} + \text{FP}} \quad (2)$$

$$\text{Recall} = \frac{\text{TP}}{\text{TP} + \text{FN}} \quad (3)$$

$$\text{F1 Score} = 2 \times \frac{\text{Precision} \times \text{Recall}}{\text{Precision} + \text{Recall}} \quad (4)$$

where A represents the area of the UAV-extracted building footprint, B represents the area of the corresponding OSM building footprint, TP (true positives) are correctly identified buildings, FP (false positives) are nonbuilding areas incorrectly identified as buildings, and FN (false negatives) are buildings that were not identified in A.

This comparison provides a relative measure of agreement with an independent dataset; however, it should not be considered ground truthing. Since OSM data are contributed by a global community of mappers, it is subject to certain limitations and potential biases. The custom house polygon extraction, combined with manual refinement, allows for a much finer level of control over the building footprint geometries and their alignment with the underlying elevation data. This tailored approach was considered more suitable for this study, as building footprints derived directly from the high-resolution UAV-based DSM are expected to align more

accurately with the study's elevation data than the more general OSM dataset, which served primarily for an independent comparative assessment.

3.5. Snow depth analysis around infrastructure

To investigate the spatial distribution of snow depth in proximity to buildings and roads, buffer zones were created around these features. These buffers allow for the extraction of snow depth statistics from the elevation difference raster (September 2022 to March 2024) in areas directly influenced by infrastructure. A 1 m outward buffer to each building polygon was applied to exclude the immediate vicinity of the structure. This exclusion was necessary to mitigate observed edge artifacts in the DSM, where vertical building walls caused elevation distortions that extended slightly beyond the true footprint. From the outer edge of this 1 m buffer, a further 5 m buffer was extended. This 5 m width was selected to capture the primary extent of snowdrifts induced by the structure, while minimizing potential overlap with the influence zones of adjacent buildings.

For the delineated road network, a two-stage buffering process was applied. First, a 4 m buffer was created on each side of the OSM road polyline, corresponding to the approximate half-width of the cleared road surface. This excludes the area expected to be free of snow accumulation. From the outer edge of this 4 m buffer, a subsequent 5 m buffer was extended outwards, creating a zone of interest for analyzing snow accumulation adjacent to the cleared roadway. To allow for a more granular analysis of snow depth variations, the road buffer polygons were segmented into max. 50 m long sections (min. 12 m) along the road network. The road buffer polygons were further classified into four directional sectors (N, S, E, and W), to assess the symmetry of snow distribution across road embankments, based on their orientation relative to the road centerline. For each building buffer and each road segment buffer, the pixel values from the elevation difference raster were extracted. From these extracted pixel values, the mean, median, and standard deviation were calculated. These statistics provide a quantitative summary of the snow depth distribution within each buffer zone, representing the central tendency and variability of snow accumulation around each building and along each road segment. These buffered zones, with associated snow depth statistics, form the basis for subsequent analyses of snow insulation impact on the underlying permafrost.

3.6. Potential snow insulation

To demonstrate the utility of high-resolution snow depth maps for infrastructure risk assessment, we estimated the potential insulating effect of the snowpack. This approach calculates a snow damping factor (n_f) and the resulting potential surface temperature offset (ΔT_s) following the steady-state approach of Slater et al. (2017). The full mathematical derivation, including the governing equations and parameterization details, is provided in Appendix C.

The model approximates the effective snow depth (S_{eff}) by scaling the March 2024 UAV-derived depth (h_s) with a seasonal scaling factor ($\alpha \approx 0.70$), derived from historical daily snow depth data (2010–2020) for Aklavik (Brown and Brasnett 2010). This accounts for the accumulation and persistence of the snowpack over the winter season.

A critical variable in this assessment is snow density, which dictates thermal diffusivity (κ). Snow accumulation around infrastructure in Arctic communities is a complex composite of wind-driven redistribution and human management. To account for the resulting compaction, we applied a simplified binary classification. Pixels falling within the infrastructure mask (roads and building perimeters) were assigned properties of compacted snow ($\rho = 450\ kg/m^3$), while open areas were assigned properties of soft, wind-slab snow ($\rho = 230\ kg/m^3$). These values are estimates based on literature values for Arctic environments and infrastructure snow banks (Sturm et al. 1997; Zhao et al. 2023). The resulting map of ΔT_s represents the potential bias induced by the snow cover on the Mean Annual Ground Surface Temperature (MAGST) relative to the air temperature.

4. Results

4.1. Accuracy of the snow depth map

4.1.1. DSM data alignment

The effectiveness of the alignment process is demonstrated by the reduction in observed offsets at 20 independent check points. Initially, the DSMs exhibited a mean horizontal offset (bias) of −1.43 m in X and +0.10 m in Y (refer to Fig. 3), with RMSE values of 1.76 and 1.02 m, respectively. The vertical offset (Z) was considerably larger, with a mean bias of 4.18 m and an RMSE of 4.53 m. The ICP alignment step significantly improved the alignment in all dimensions. It adjusted the horizontal offsets to a mean bias of −0.46 m in X (RMSE 0.65 m) and +0.16 m in Y (RMSE 0.56 m). The vertical alignment was also substantially improved, reducing the Z-offset bias to −0.53 m and the RMSE to 1.26 m. The subsequent Kriging correction, which specifically targeted residual vertical errors, further refined the Z alignment, resulting in a final mean bias of −0.02 m and an RMSE of 0.21 m for the vertical dimension. The horizontal offsets remained unchanged by this Kriging process as it only adjusted Z values. The resulting kriged offset map revealed a smooth, low-frequency gradient, contrasting with the high-frequency variability of the snow depth map. This confirms that the correction targets global alignment errors without smoothing localized snow accumulation features.

4.1.2. Comparison with in situ data

Figure 4 presents a scattar plot that compares the UAV-derived snow depths to the corresponding in situ measurements. The accuracy analysis includes 30 of the 44 measurement sites, located within the 0.98 km^2 area of overlap between the September 2022 and March 2024 survey extents. The remaining 14 measurements—located in the western part of Aklavik—had to be excluded due to the uncorrectable vertical errors in the 2022 data (see Section 3.1).

Fig. 3. Comparison of *X*, *Y*, and *Z* offsets (in meters) at 20 independent check points between the September 2022 reference digital surface model (DSM) and the March 2024 DSM at different stages of alignment: initial uncorrected offsets (indigo blue), offsets after ICP-only correction (teal), and after combined ICP and Kriging correction for the *Z* dimension (light green). ICP, iterative closest point.

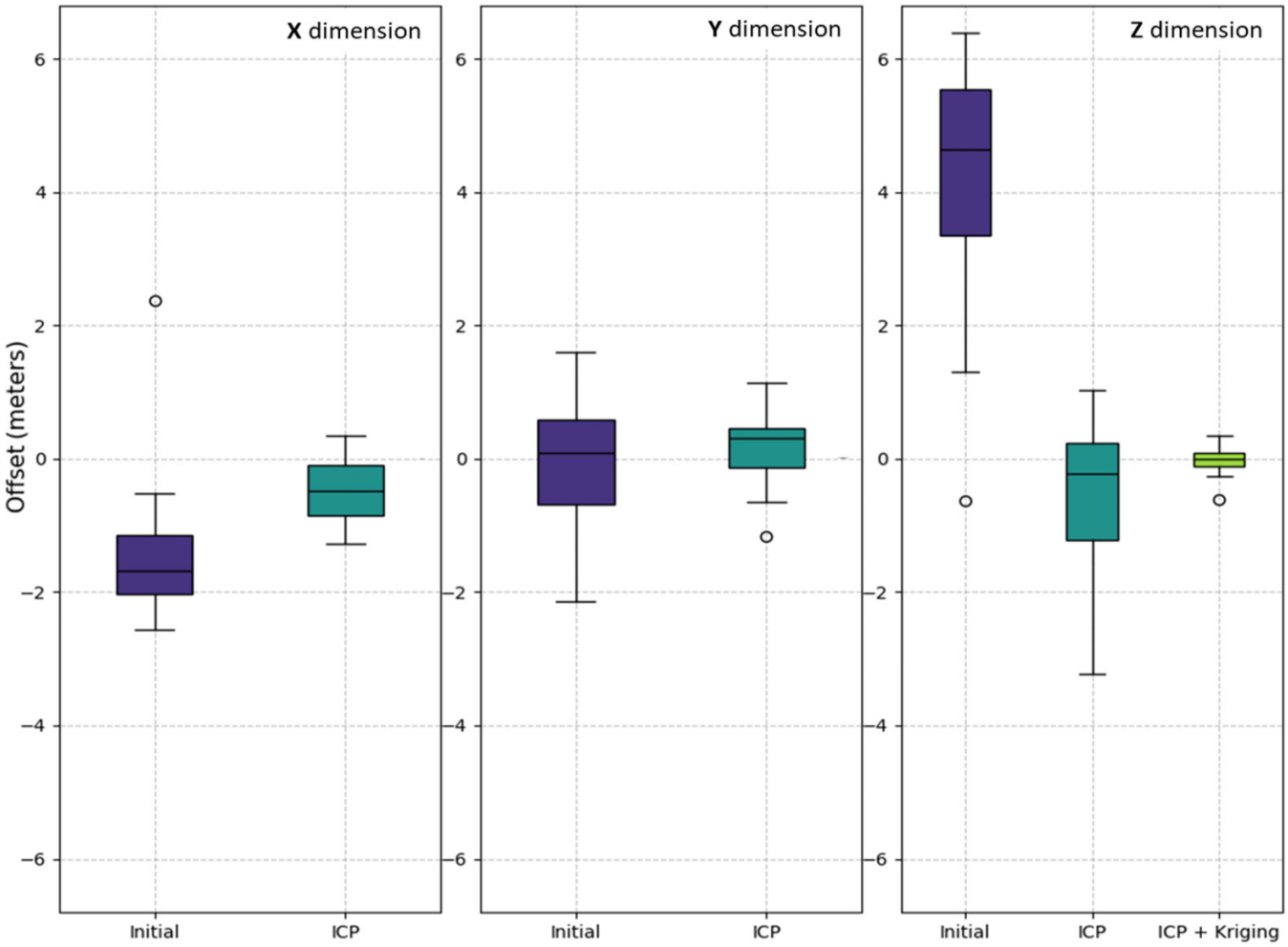

The in situ snow depth measurements ranged from 0.16 to 1.16 m, while the UAV-derived measurements ranged from 0.04 to 1.15 m. The coefficient of determination (R^2) between the two datasets was 0.35, indicating a moderate linear relationship. A bias of −17.32 cm and an RMSE of 30.45 cm were observed, suggesting a systematic underestimation of snow depth by the UAV-based method compared to the in situ probe measurements. Comparing the measurements by dominant land cover type (determined through visual inspection of the September 2022 orthomosaic) reveals important trends related to measurement accuracy. Sites located on bare soil (brown squares) and water surfaces (blue circle) exhibited moderate agreement between in situ and UAV-derived snow depths, generally clustering close to the 1:1 line. Sites dominated by low grass vegetation (light green triangles) also showed relatively good agreement, though with a greater degree of scatter. However, a more pronounced underestimation by the UAV method was observed at sites characterized by higher shrub vegetation (dark green crosses). With the removal of high vegetation measurement location, R^2 increases to 0.46, bias and RMSE decrease to −6.7 and 20.7 cm, respectively. Higher RMSE values were consistently observed in areas characterized by dense shrub canopies.

4.1.3. Comparison with snow-cleared roads

To provide an independent assessment of systematic biases in the snow depth map, an internal validation was performed using the OSM road centerlines. These roads, maintained with a compacted ice layer of ≤1 cm as verified by manual probing, served as a baseline for zero snow depth. Figure 5 displays the distribution of these extracted pixel values, representing the residual elevation differences along the roads. A total of 1.9 million road pixel values were extracted (1 m buffer around centerlines) and analyzed. The distribution exhibits a positive skew, with a mean offset of 10.99 cm and a median offset of 8.24 cm. The 10th and 90th percentile values were −5.72 and 33.17 cm, respectively, with a standard deviation of 21.64 cm. This observed median offset, while indicating a slight systematic positive bias, is relatively small

Fig. 4. Scatter plot comparing in situ snow depth measurements ($n = 30$) with corresponding UAV-derived snow depth estimations. UAV-derived values represent the median snow depth within a 2 m buffer around each in situ measurement location. Points are distinguished by dominant land cover type using specific colors and markers. Statistical metrics are provided separately for the full dataset (top left) and for the subset excluding high shrub sites (bottom right) to highlight the systematic underestimation caused by dense shrub canopies (dark green "X" markers). RMSE, root mean square error; UAV, unoccupied aerial vehicle.

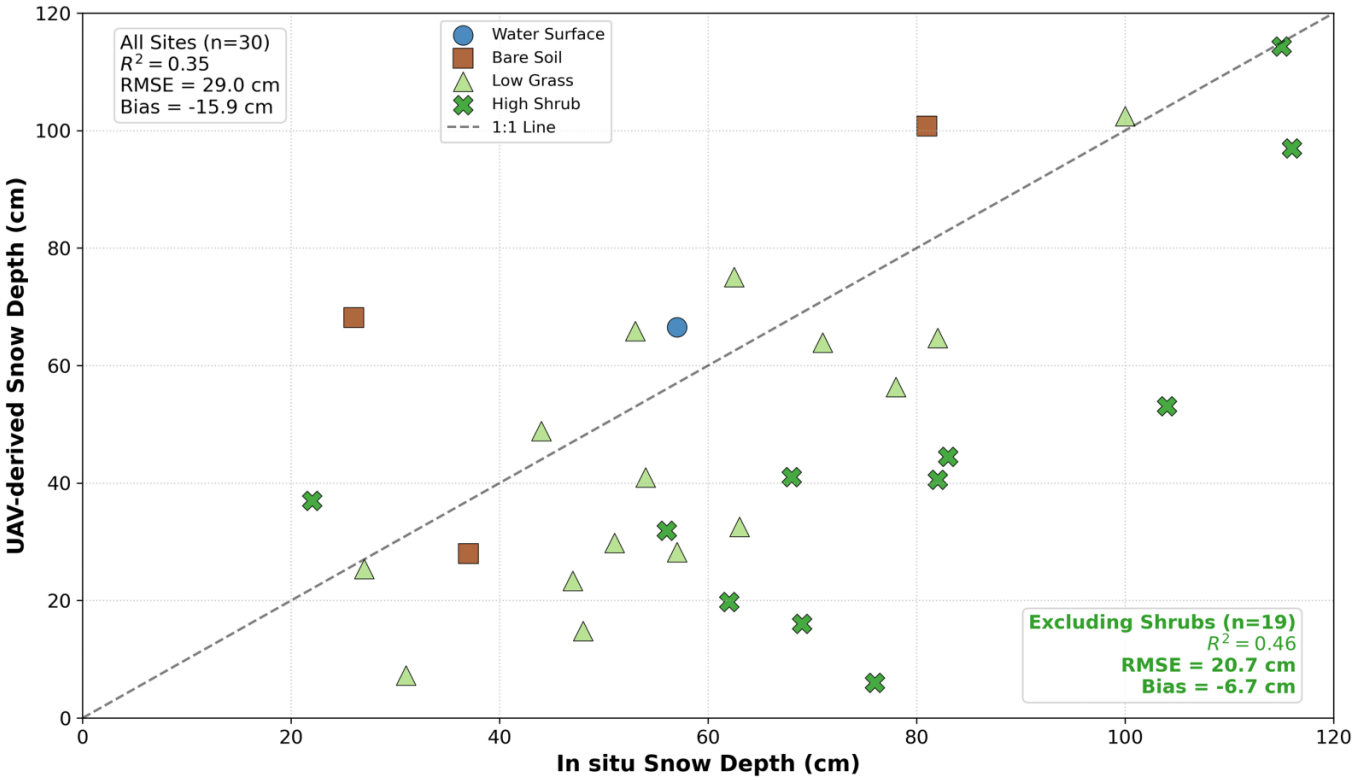

and suggests a good overall co-registration of the multitemporal datasets over these stable, bare surfaces.

4.2. Spatial distribution of snow depth

The snow depth map, derived from the difference between the September 2022 and March 2024 DSMs, provides a comprehensive overview of snow accumulation across the 0.98 km^2 study area in Aklavik (Fig. 6). We excluded values outside the range 0–2 m based on maximum snow depths observed in the field, values exceeding this threshold were identified as artifacts (e.g., moving vehicles) rather than physical snow accumulation. Negative values are generally close to zero and indicate areas where the March 2024 surface was lower than the September 2022 surface—likely due to minor remaining inaccuracies in the DSM alignment, or potential compaction or removal of surface material. Positive values above 2 m likely represent data errors or not snow-related elevation change from buildings or vegetation.

The distribution of these snow depths is visualized in Fig. 7. The descriptive statistics reveal a mean snow depth of 0.65 m and a median of 0.56 m. The distribution is wide, with values ranging from 0.02 m (2nd percentile) to 1.86 m (98th percentile), which indicates considerable spatial variability of snow depth across the landscape. The standard deviation of 0.71 m indicates considerable variability of snow depth across the landscape within the considered range. The histogram also shows a clear positive skew, with a long tail representing areas of deeper snow accumulation.

Analysis of the snow-covered area revealed that 91.1% of the study area was covered by snow (>10 cm). Crucially for permafrost insulation, over half the area (54.7%) exceeded a snow depth of 0.5 m, while deep snow accumulations (>1 m) covered 17.3% of the terrain.

4.3. Infrastructure mapping

The building segmentation yielded 291 polygons representing potential building footprints within the study area subset. These extracted footprints ranged in area from 15.11 to 3528.25 m^2, with a mean of 130.41 m^2 and a median of 86.97 m^2, exhibiting considerable size variability (standard deviation: 284.80 m^2). For comparison, the manually aligned OSM data for the same area contained 269 building polygons. To assess the agreement between the extracted building footprints and the aligned OSM data, standard metrics including IoU, precision, recall, and F1 score were calculated. This resulted in a median IoU of 0.630 for matched buildings, an overall precision of 0.834, recall of 0.653, and an F1 score of 0.733.

Fig. 5. Histogram of elevation differences extracted from within 1 m buffers around the OpenStreetMap road centerlines. The red dashed line indicates the mean offset (10.99 cm), and the blue solid line indicates the median offset (8.24 cm).

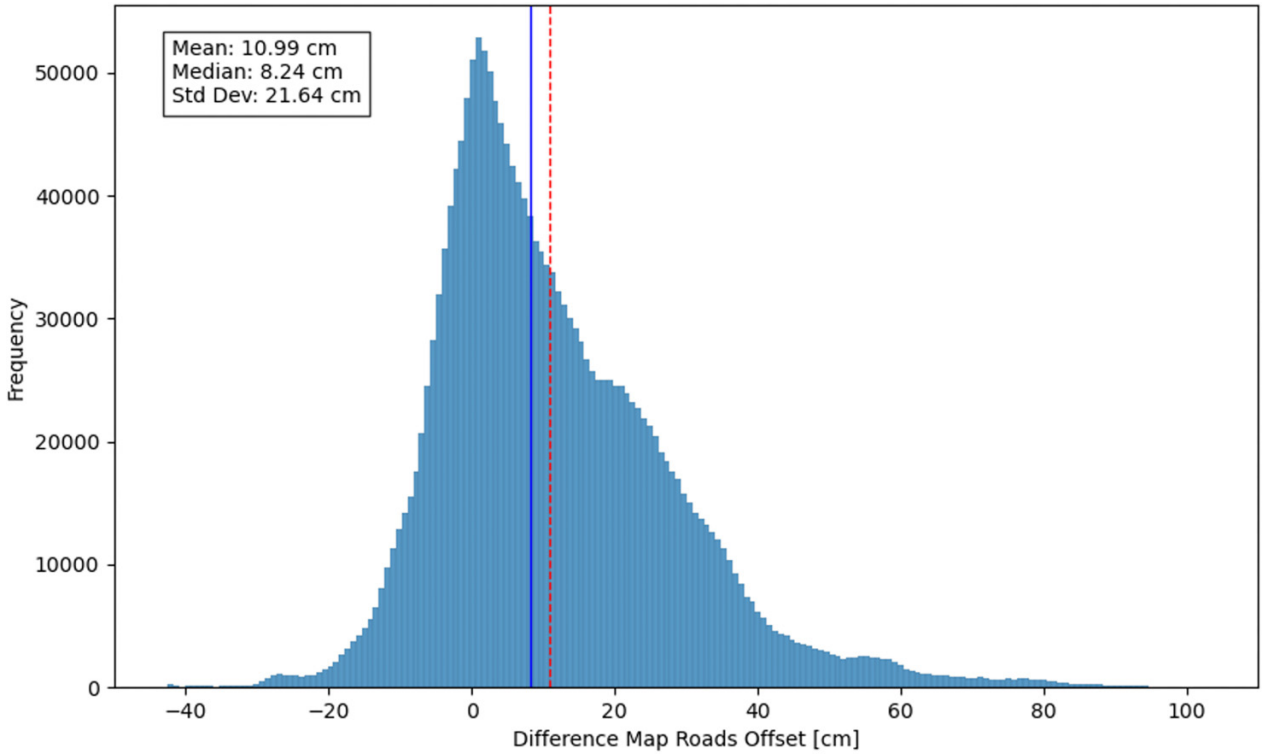

4.4. Snow depth around infrastructure

To analyze the spatial distribution of snow depth in proximity to infrastructure, buffer zones were created around building footprints ($n = 291$) and segmented road centerlines ($n = 340$ sections), as described in Section 3.4. House buffers, representing areas within 5 m of buildings (excluding the immediate 1 m perimeter), and road buffers, representing areas within 5 m adjacent to a 4 m representation of the cleared road surface on each side, were generated. Figure 8 presents the combined distribution of mean and median snow depths extracted from both the house and road buffer zones.

The overall mean snow depth was 0.59 m for house buffers and 0.65 m for road buffers. Similarly, considering the median snow depths, the overall median was 0.47 m for house buffers and 0.59 m for road buffers. The distributions of these statistics (both for mean and median snow depths) exhibited comparable overall standard deviations between houses and roads, ranging from 0.23 to 0.26 m, indicating a similar degree of variation in average snow conditions among the different instances of each buffer type. Furthermore, the average of the local standard deviations calculated within each individual house polygon segment, an indicator of snow depth heterogeneity at a fine scale was 0.44 and 0.41 m for polygon segments adjacent to roads. These findings quantify distinct snow accumulation characteristics: snow tends to be deeper on average adjacent to road corridors compared to the perimeters of buildings. Although the magnitude of this difference (6 cm) is below the individual product RMSE (≈20 cm), the spatial aggregation of measurements yields a standard error of the mean (SEM) of only 1.4 cm, confirming the separation is statistically significant (*t*-test, $p < 0.01$). Concurrently, the local variability of snow depth within individual building buffer zones appears slightly more pronounced on average than within the road buffer segments. The analysis of road embankments revealed a distinct asymmetry in snow distribution based on orientation. Areas on the South side of road embankments exhibited the highest mean snow depths (0.77 m), significantly deeper than those on the North (0.66 m), East (0.60 m), and West (0.60 m) sides (Mann–Whitney U, $p < 0.001$; see Appendix A). The lowest snow depths were observed in the East and West sectors, which showed no significant difference from each other. As the snow-induced surface temperature bias (ΔT_s) is a direct function of snow depth (see Section 3.6), these differences in accumulation also represent a corresponding difference in thermal insulation, the spatial patterns of which are detailed in the following section (Fig. 9).

4.5. Snow insulation potential

The spatial distribution of the potential snow-induced temperature offset (ΔT_s) within the infrastructure buffer zones is presented in Fig. 9. Based on the weather station data for the preceding year (mean annual air temperature, MAAT −5.8 °C), the model suggests that the snowpack introduces a theoretical warming potential ranging from negligible (≈0 °C) in snow-free areas up to ≈6.5 °C in areas of deep accumulation.

Visually, high ΔT_s values (orange and red in Fig. 9) track the linear patterns of snow accumulation adjacent to roads

Fig. 6. Snow depth map of Aklavik, derived from the difference between the September 2022 and March 2024 DSMs. Buildings were delineated using the watershed algorithm and excluded here. Background: OpenStreetMap basemap. DSMs, digital surface models.

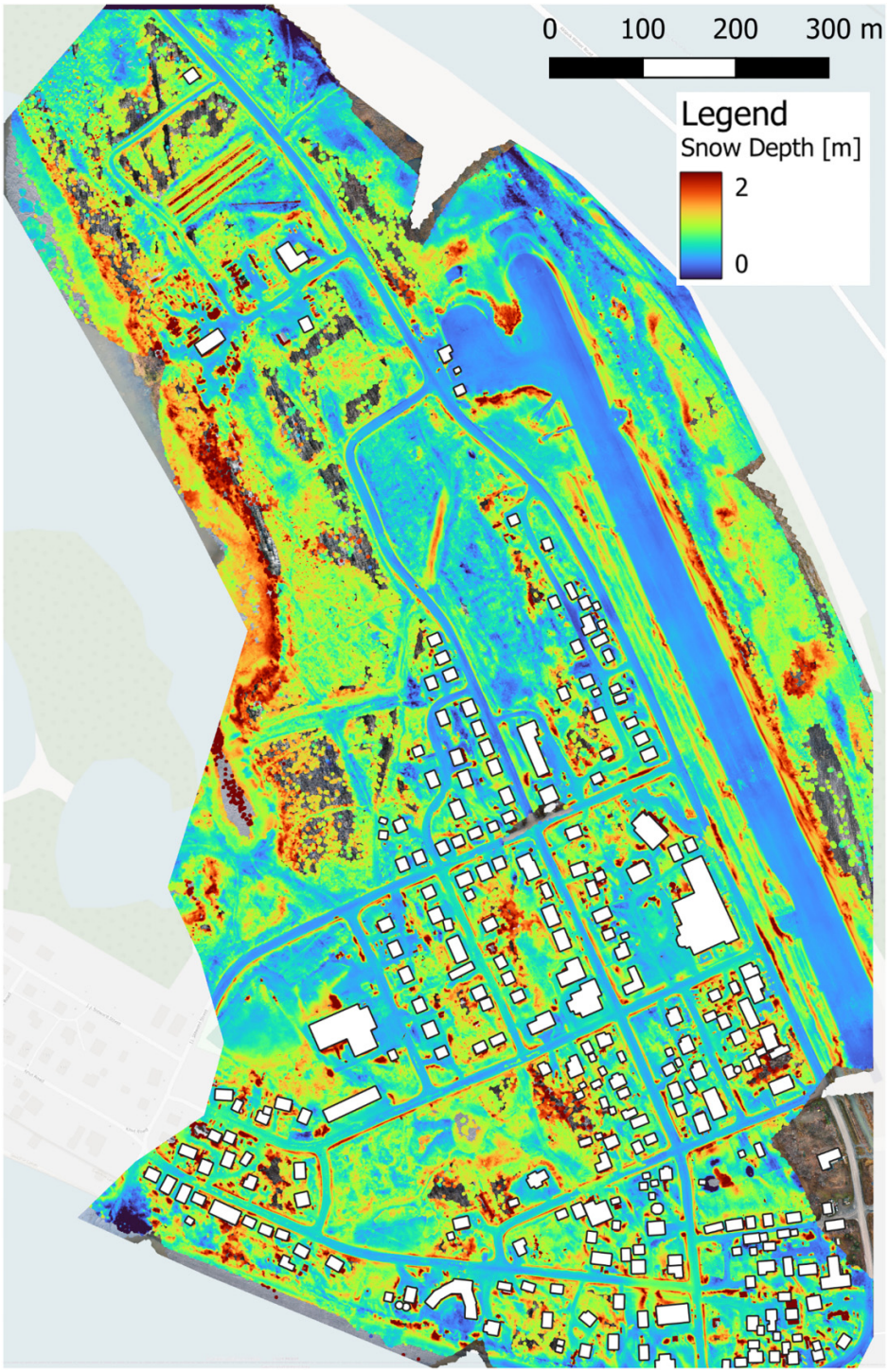

and the airstrip. These features result from snow clearing and piling activities, creating localized zones of deep insulation. This highlights the capacity of human snow management to inadvertently increase thermal stress on the underlying permafrost.

The analysis of the potential temperature offset provides insight into the relative differences between infrastructure types. For road buffer segments ($n = 340$), nearly half (45%) exhibited a mean warming potential of >2 °C. Notably, roughly 6% of road segments showed very strong insulation with mean offsets >3 °C. In contrast, residential areas showed slightly lower potential impacts; only 35% of house buffer polygons ($n = 291$) had a mean $\Delta T_s > 2$ °C, and 2% exceeded 3 °C.

Fig. 7. Histogram of the snow depth distribution across the study area with mean and median snow depth marked as vertical lines. For clarity and to exclude outliers, the chart displays pixel values between the 2nd and 98th percentiles.

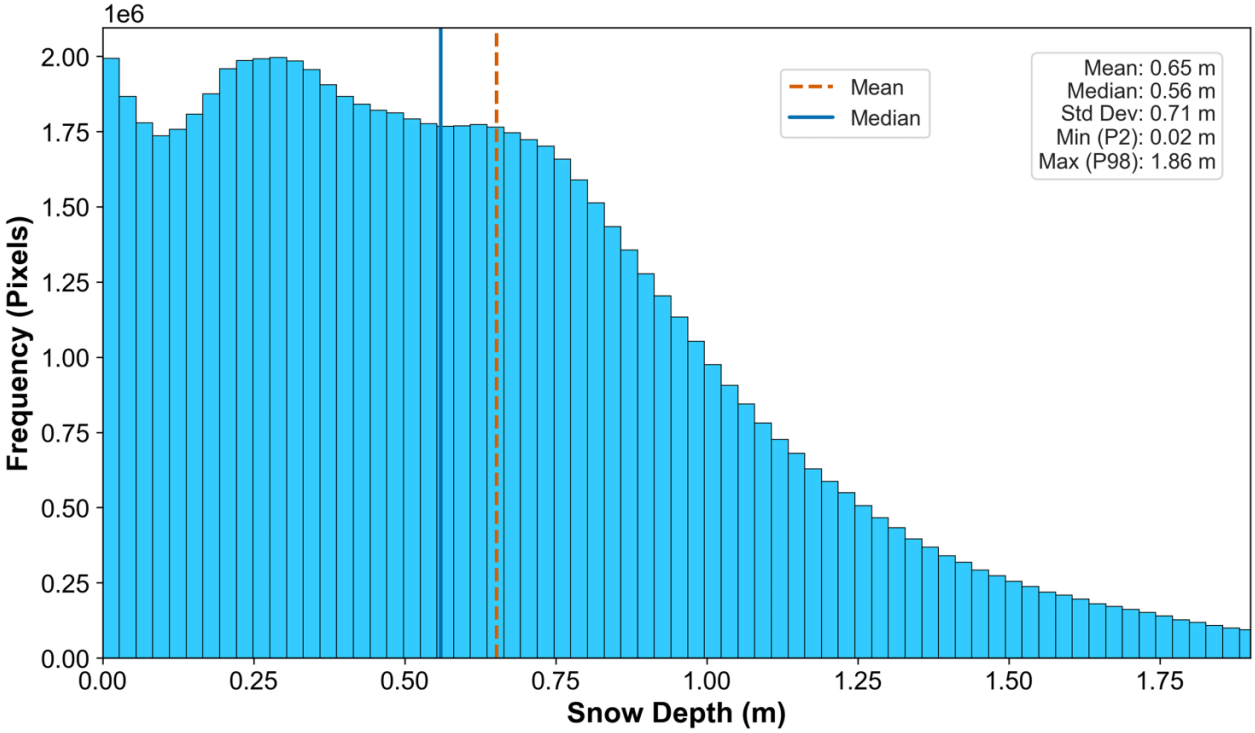

These results indicate that while both infrastructure types are subject to insulation, road embankments are subject to a higher projected warming bias compared to residential perimeters. While these values represent a first-order approximation, they demonstrate how the workflow can spatially identify warming hotspots that may require maintenance or adaptation measures.

5. Discussion

5.1. Performance and methodological considerations of UAV-derived snow depth

The internal validation using snow-cleared roads offered a valuable perspective on the effectiveness of the co-registration process. Through the applied ICP alignment and subsequent Kriging-based correction, the median offset on these presumed zero-snow-depth areas was successfully reduced to +8.24 cm in the difference map (Fig. 5). Furthermore, residual horizontal offsets (≈0.5 m) between the datasets may contribute to propagated vertical errors, particularly in areas with steep snow depth gradients, although this effect is likely within the positional uncertainty of the validation measurements themselves. It should be noted that achieving such a small residual vertical error (i.e., <10 cm) is indicative of a very accurate alignment, especially considering the consumer-grade UAV hardware utilized in this study (Mueller et al. 2023). This result demonstrates that even with the challenges of non-RTK GNSS and a partially subjective alignment workflow, the chosen methodology is robust for producing high-quality multitemporal datasets. Furthermore, while winter illumination conditions pose a challenge for photogrammetric reconstruction, the multiangle spiral flight path provided sufficient point cloud density to support the subsequent alignment and differencing steps.

The comparison between UAV-derived snow depth estimations and in situ probe measurements revealed a moderate correlation ($R^2 = 0.35$) with a notable systematic underestimation by the UAV method (bias = −17.32 cm and RMSE = 30.45 cm) when all vegetation types were included. These accuracy metrics are consistent with a comparable SfM snow depth study Maier et al. (2022), who reported RMSEs ranging from 11.5 to 41.0 cm under varying environmental conditions. This discrepancy is primarily attributed to the influence of vegetation, a known challenge in SfM-based surface reconstruction (Lamare et al. 2023). The UAV-derived snow depth represents the difference between the snow surface elevation captured in March 2024 and the apparent surface elevation from September 2022.

In areas characterized by substantial shrub cover, the SfM algorithm reconstructs the visible surface, which corresponds to the top of the vegetation canopy rather than the true ground level (Harder et al. 2020). Consequently, subtracting this elevated reference surface from the winter surface leads to a systematic underestimation of the snow depth. Attempts to filter this vegetation were unsuccessful due to the leaf-on conditions and sensor specifications (12 MP at 120 m AGL), which resulted in a complete occlusion of the ground in dense shrub areas. The in situ probe measurements are unobstructed by vegetation and reach the ground, measuring the total snow depth (Vander Jagt et al. 2015). While the sample size ($n = 30$ within the overlap area) limits the statistical robustness of land-cover-specific subanalyses, the points cover the full range of observed surface types. Consequently,

Fig. 8. Comparative frequency distributions for individual house and road buffer zones. The histogram displays the median snow depth (m, top *x*-axis) and the corresponding derived snow-induced surface temperature bias (ΔT_s, in °C, bottom *x*-axis). This dual-axis representation illustrates both the physical snow accumulation patterns and their potential thermal impact.

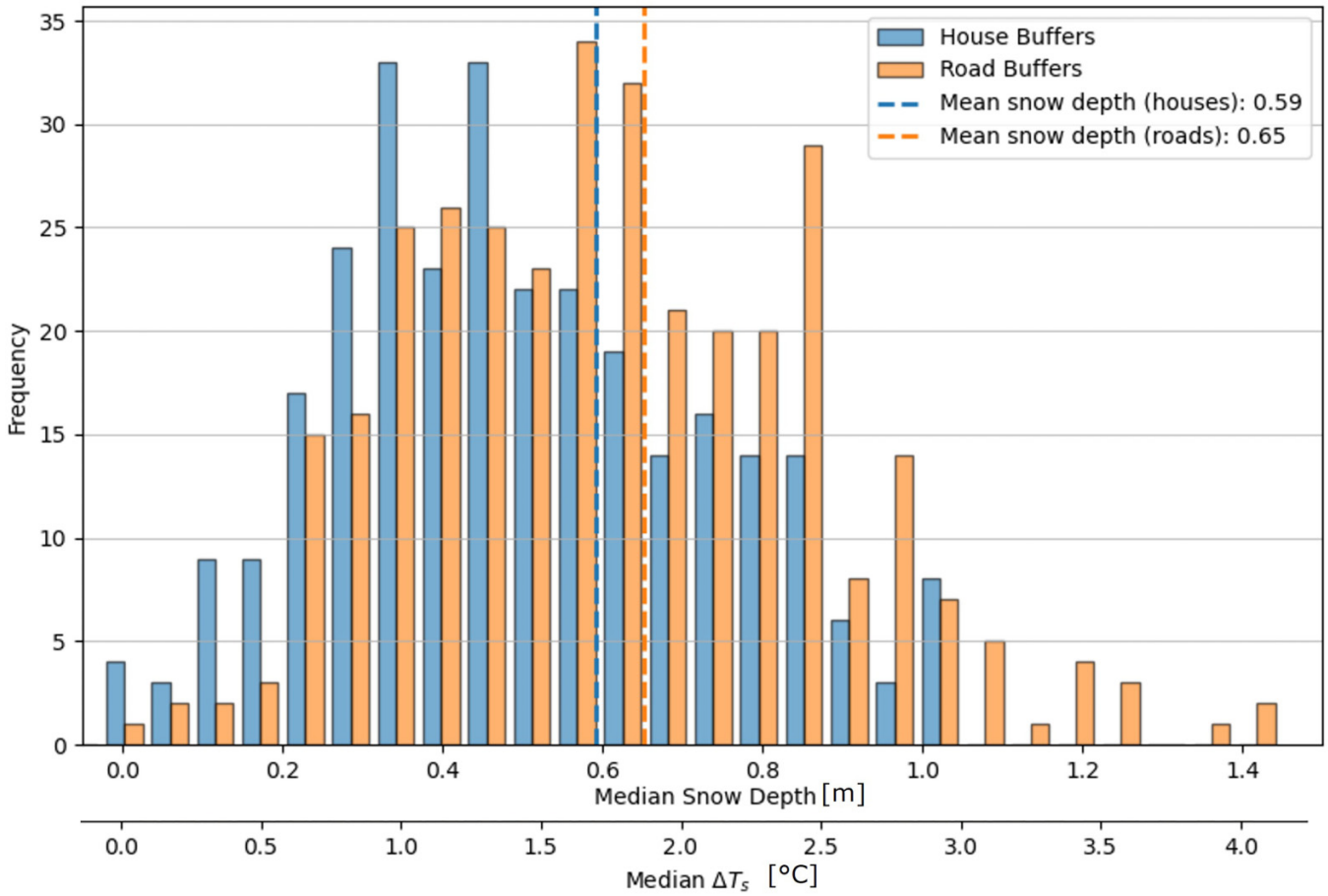

where the snow-free DSM captures vegetation height, the resulting snow depth difference calculated using the snow-covered DSM inherently underestimates the true snow depth. This effect is evident in the qualitative analysis (Fig. 4). While the limited number of points on bare soil or water prevents robust statistical conclusions, they generally cluster closer to the 1:1 line compared to vegetated sites. Points in low grass show increased scatter and a slight negative bias, indicating that even lower vegetation can obscure the true ground level. Points in higher shrub vegetation exhibit the most substantial underestimation by the UAV approach. Approximately 37% of our validation sites were situated in these shrub-dominated areas, where the underestimation is most pronounced. Even though there is substantial shrub coverage across the natural landscape, the specific zones of interest for this study, the immediate buffers around roads and buildings, are subject to vegetation management and consequently exhibit lower shrub density. Removing measurement locations dominated by higher vegetation improved the correlation ($R^2 = 0.46$) and reduced the bias (–6.7 cm) and RMSE (20.7 cm), further supporting the substantial impact of vegetation structure on accuracy.

Understanding the small positive offset on cleared roads provides a valuable framework for interpreting the overall snow depth map. While this +8.24 cm median offset indicates a persistent slight systematic overestimation on bare ground, likely due to residual compacted snow or ice glazing remaining after clearing combined with minor residual alignment imperfections and slight physical changes to the unpaved road surfaces (Batenipour et al. 2012; James et al. 2019; Berra and Peppa 2020), its primary value lies in how it informs the data's application. Since the roads are assumed to be snow-free, any positive elevation difference observed on them can be considered when assessing snow elsewhere. Consequently, particularly for vegetated areas, the snow depth values derived from the UAV-SfM approach can be interpreted as representing a minimum snow depth across the study area. This value signifies either the approximate true snow depth over bare ground (potentially including the slight overestimation) or, more conservatively, a lower bound on the actual snow depth in vegetated areas. This interpretation allows for a conservative, yet spatially comprehensive, assessment of snow cover from the UAV data. It is a critical methodological outcome, as for infrastructure risk assessment, knowing the minimum insulating snow depth provides a reliable and cautious baseline.

Regarding the infrastructure mapping, the semi-automated building extraction showed a reasonable level of agreement with OSM data. The observed higher precision compared to recall suggests that the extracted footprints are

Fig. 9. Spatial distribution of infrastructure-adjacent accumulated snow depth (m) and the corresponding potential snow-induced surface temperature offset (ΔT_s, in °C) for March 2024 in Aklavik. The main map (*a*) shows the buffer zones around all buildings and roads, while the inset (*b*) provides a detailed view. The legend indicates the corresponding value ranges. Background: OpenStreetMap basemap.

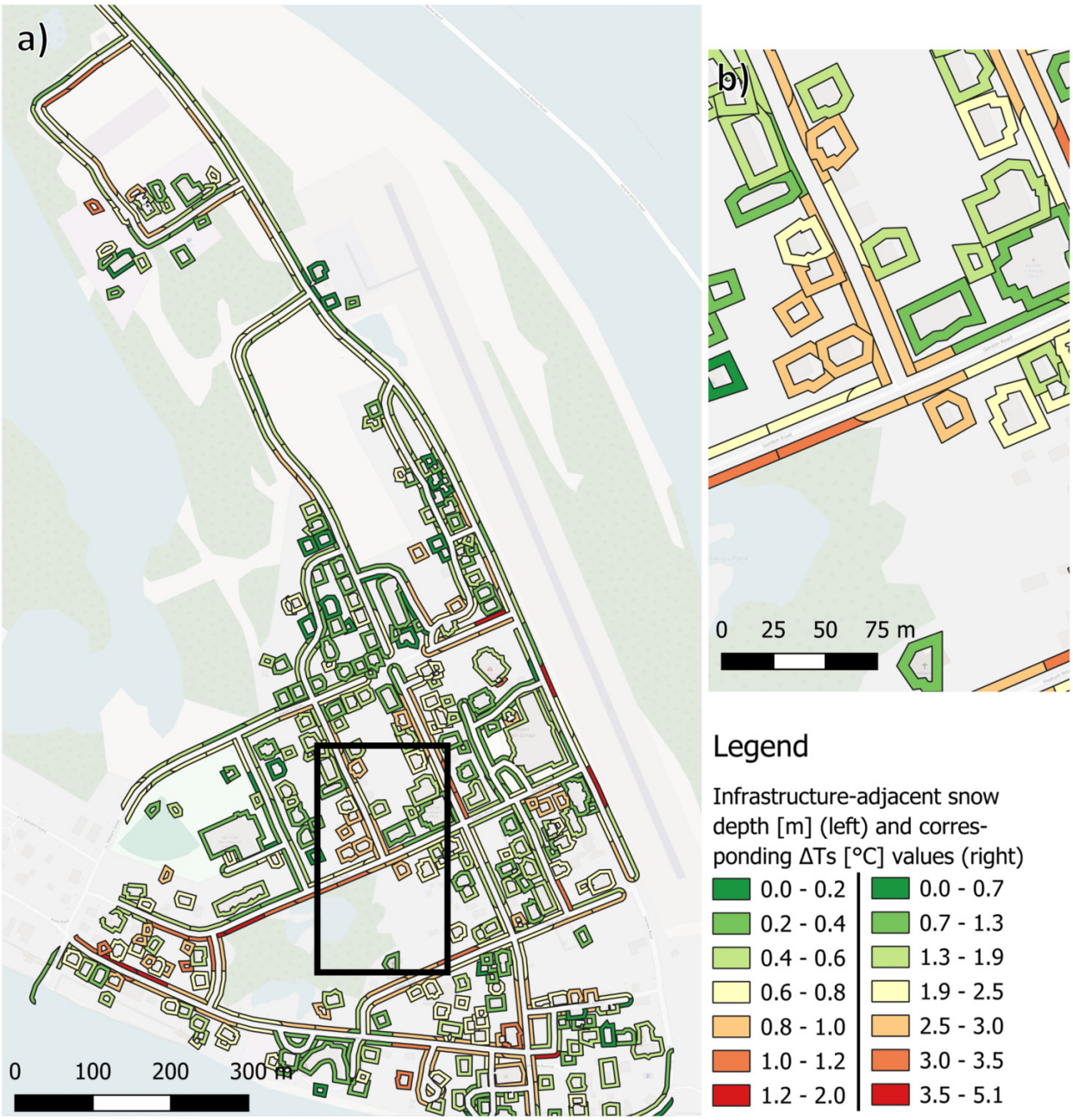

generally accurate where they overlap with OSM buildings. However, the lower recall indicates that some OSM buildings were not detected by the automated method. This trade-off was deemed acceptable as the primary goal was to identify valid building-adjacent zones for snow depth analysis rather than a perfect cadastral map.

5.2. Quantifying snow insulation effects using high-resolution UAV data

A primary contribution of this study is the translation of the high-resolution snow depth map into a spatially explicit map of the snow-induced surface temperature bias (ΔT_s) at a resolution relevant to infrastructure assessment. The interpretation of this map is informed by several methodological considerations. First, the accuracy of the final thermal map is directly dependent on the accuracy of the input UAV-derived snow depth map (h_s). As discussed in Section 5.1, this leads to a conservative estimate of insulation in densely vegetated areas, and a more representative estimate on bare, stable surfaces like roads. Second, the calculation relies on a practical approach for landscape-scale analysis, using generalized snow thermal properties. Fixed thermal diffusivity val-

ues (k_{map}) based on a binary classification (compacted snow near infrastructure vs. soft snow elsewhere) are derived from established empirical relationships (Sturm et al. 1997). While actual snowpack thermal properties exhibit considerable heterogeneity (Mellor 1977; Dutch et al. 2022), this approach effectively captures the first-order effects of anthropogenic compaction. Consequently, this steady-state metric reflects the mean seasonal insulation potential and does not resolve short-term thermal fluctuations caused by wind variability or transient weather events. Future work incorporating in situ snow density measurements would allow for site-specific tuning of these properties. Thirdly, the methodology uses a simplified approach to temporal dynamics, approximating the seasonal evolution of the snowpack with a historical accumulation factor (α) and single-station temperature data, in order to maintain a primary focus on the high-resolution spatial variability of snow's thermal impact. The precision of these thermal indices could be further enhanced in the future by integrating site-specific temporal data, for example from continuous in situ snow monitoring (Aga et al. 2025).

The resulting spatially distributed ΔT_s map holds considerable potential. It translates the high-resolution snow depth information into a metric directly relevant to permafrost thermal stability. Its primary strength lies in revealing the relative spatial patterns of insulation potential around infrastructure. It enables the identification of potential "hotspots", areas adjacent to buildings or roads characterized by deep snow and consequently high ΔT_s values, which may correspond to zones of increased risk for localized permafrost thaw (Gisnås et al. 2016). As demonstrated (Section 4.5), this allows for quantitative comparisons of average insulation potential between different infrastructure types. This spatially explicit, albeit simplified, value can serve as a valuable input for parameterizing or validating more sophisticated numerical ground thermal models and provides a tangible tool to inform discussions and decisions regarding targeted monitoring, infrastructure maintenance, and adaptive snow management strategies within Arctic communities. Crucially, the application of low-cost UAV systems, as demonstrated in this study, opens the possibility for more frequent monitoring of snowpack evolution, which can lead to a more dynamic and refined assessment of snow insulation patterns over time.

The importance of these "hotspots" is clear when considering the direct thermal impacts on the ground surface, quantified by the reduction in accumulated freezing degree-days (FDD_s) relative to air temperatures (FDD_a). This reduction, indicated by positive ΔT_s values (which ranged up to 6.5 °C in this study as shown in Section 4.5), translates to effectively warmer conditions at the ground surface during the freezing season. Such snow-induced surface warming is a critical factor when assessing the stability of underlying permafrost, especially as mean annual ground temperatures (MAGT) below −5 °C are often considered indicative of stable permafrost, while MAGT warmer than −2 °C may be metastable and highly sensitive to thermal changes (Harris 1986). The MAAT for the specific year used to derive the FDD_a for the ΔT_s calculation was −5.84 °C. This proximity to the −5 °C threshold underscores the general thermal sensitivity of the area. Consequently, the additional surface warming from snow insulation can be particularly critical in pushing local ground thermal regimes towards less stable temperature ranges. The findings that over 45% of road segments and nearly 35% of house buffer polygons experienced a mean $\Delta T_s > 2.0$ °C underscore this impact. A high ΔT_s indicates an increased thawing sensibility of the permafrost under engineering activities (Qingbai et al. 2002), potentially accelerating thaw and increasing risks to infrastructure integrity. Therefore, the high-resolution ΔT_s information derived from the UAV data serves as a crucial tool for identifying specific infrastructure sections that may be particularly vulnerable to these snow-related thermal impacts.

5.3. Operationalizing low-cost UAVs in Arctic environmental monitoring

The potential of this low-cost UAV approach is substantial. It dramatically reduces the financial barrier compared to traditional airborne surveys (LiDAR or large-format cameras) or TLS campaigns, making frequent, high-resolution monitoring feasible for local communities and researchers. The operational flexibility allows for timely data acquisition synchronized with specific events or conditions. The generated cm-scale resolution data is highly relevant for analysing snow distribution around individual buildings and infrastructure elements, a scale often unresolved by satellite data or feasible with extensive manual probing. This methodology offers a scalable tool for understanding fine-scale snow processes critical for infrastructure stability assessments.

However, operationalizing this approach in Arctic community environments requires acknowledging practical constraints. Weather conditions, for instance, can pose limitations, UAV operations are constrained by factors such as low temperatures affecting battery life, high winds impacting flight stability, and suitable lighting for photogrammetry (Mueller et al. 2023). Furthermore, the sensitivity of low-cost GNSS systems to signal quality issues in high latitudes remains a consideration, as encountered in two of the 2022 flights (Swaszek et al. 2018). From a data processing perspective, the multistep workflow, involving SfM processing, point cloud alignment, interpolation, and differencing, currently requires considerable manual intervention and expertise. This presents the primary challenge for direct implementation by communities without specialized training and software access (Mamun and Natcher 2023).

Future improvements can address these operational challenges and enhance the method's accessibility. Integrating accurately surveyed GCPs or utilizing PPK/RTK-enabled low-cost UAVs could enhance georeferencing accuracy and reduce reliance on post-processing alignment, although this increases cost and logistical effort. Exploring advanced SfM processing techniques, potentially incorporating co-alignment of multitemporal imagery with only a few accurately mapped fix points within the SfM software, could further improve relative accuracy (Nota et al. 2022). Investigating fusion with other data sources, such as satellite imagery or thermal data, might also offer complementary insights for a more comprehensive assessment. Additionally, establishing a high-quality baseline Digital Terrain Model (DTM) using Lidar UAV systems during leaf-off conditions would allow for more accurate sep-

aration of vegetation and snow in future low-cost monitoring campaigns.

5.4. Implications for infrastructure and community-based monitoring

The detailed snow depth maps (Fig. 6) and derived thermal impact maps (ΔT_s) provide crucial information for understanding how snow interacts with the built environment and influences the underlying thermal regime. The substantial spatial variability in snow depth observed across the study area (mean = 0.54 m and std. dev = 0.48 m), and particularly the patterns identified around buildings and roads (Section 4.4), highlight areas where deep snow accumulations occur. These accumulations, resulting from both wind redistribution around structures and snow management practices like piling (Hjort et al. 2022; Landers and Streletskiy 2023), act as potent insulators that inhibit winter heat loss from the ground, potentially accelerating thaw beneath infrastructure (Manos et al. 2025). Our findings quantify this effect, showing that over 45% of road-adjacent areas and nearly 35% of building-adjacent areas experienced a mean snow-induced surface temperature bias (ΔT_s) greater than 2.0 °C. This is consistent with other site-specific studies investigating infrastructure (Cao et al. 2023). For instance, in a town in Svalbard, Aga et al. (2025) observed that artificial snow deposits from ploughing, similar to the practices in Aklavik, led to the highest Mean Annual Ground Surface Temperatures (MAGST) in the village, reaching up to +1.4 °C. During winter, this corresponded to a max. warming effect of up to 10.2 °C compared to undisturbed sites, a value comparable to the maximum ΔT_s of 6.5 °C found in our study. Similarly, both modeling and field studies of the Dalton Highway in Alaska by Schneider von Deimling et al. (2021) identified enhanced snow accumulation at the road shoulder as a key factor for increased soil temperatures, inferring an observed soil surface warming of about 4 °C due to snow insulation. These studies corroborate our finding that road corridors experience particularly enhanced insulation effects from accumulated snow, which we measured as slightly higher mean snow depth (0.65 m) compared to buildings (0.59 m). It is important to note that this assessment solely quantifies the insulation capacity of the snowpack. It does not account for anthropogenic heat leakage from building foundations, which likely acts as an additional warming source for the active layer in residential zones. Furthermore, this accumulation is not uniform; our directional analysis revealed a significant asymmetry along road embankments, with South-facing slopes accumulating deeper snow (0.77 m) compared to North-facing ones (0.66 m) ($p < 0.001$; see Appendix A). This pattern is consistent with leeward deposition driven by the prevailing Northwest winds (Klock et al. 2001), showing how infrastructure orientation relative to wind direction influences local insulation risks. On a broader scale, a pan-Northern Hemisphere analysis by Peng et al. (2024) found that the average damping of annual mean ground surface temperature due to snow is 5.06 ± 3.15 °C, placing the substantial warming effects observed in Aklavik well within the expected range for snow-rich environments. By identifying persistent snow accumulations hazardous to infrastructure stability, communities could potentially adapt snow clearing operations to minimize detrimental accumulation in critical areas, balancing the need for winter accessibility (which requires snow plowing and piling) with the objective of minimizing the ground-warming effects of these snow accumulations on permafrost. Furthermore, the high-resolution data can serve as valuable input for local-scale permafrost thermal models, improving predictions of thaw settlement and infrastructure vulnerability under future climate scenarios (Hammar et al. 2023). The need for such accessible monitoring tools is underscored by the urgency of several interconnected Arctic challenges. The widespread industrial legacy and associated contamination risks in permafrost regions, as highlighted by Langer et al. (2023), requires effective monitoring of parameters like snow cover that directly influence ground thermal regimes and thus containment stability. This urgency is amplified by pan-Arctic assessments revealing extensive coastal infrastructure vulnerability Tanguy et al. (2024), for example, project that ground temperatures at 77% of existing coastal built infrastructure will be above 0 °C by 2100 due to permafrost thaw. Integrating localized environmental monitoring from UAVs with detailed infrastructure inventories, such as the SIRIUS dataset (Synthesized Inventory of CRitical Infrastructure and HUman-Impacted Areas in AlaSka (Kaiser et al. 2024)), can substantially enhance these large-scale risk assessments and inform proactive adaptation planning.

Critically, this study demonstrates the practical application of consumer-grade UAVs for community-based monitoring programs in the Arctic (Lim et al. 2022; Gleason et al. 2023; Wilson et al. 2024). Specifically, the use of a readily available, sub-250g drone shows that the data acquisition phase can be accomplished with minimal technical training and cost. This was demonstrated by the successful collaboration with the Moose Kerr School in Aklavik as part of the "UndercoverEisAgenten" project (Walz et al. 2025), where community members, alongside project scientists, collected scientifically valuable imagery also utilized in the present study. While it may be unrealistic to expect community members to perform the entire complex workflow, the critical achievement is the empowerment of local residents in the data collection itself (Pedersen et al. 2020). This approach fosters local capacity and enables a monitoring continuity and frequency often difficult for external research campaigns to achieve. A collaborative model, where communities lead the flexible and timely field data acquisition while partnering with researchers for data processing, therefore presents a viable path forward. This collaborative approach ensures that the technology serves local needs effectively, contributing to informed decision-making for climate adaptation and sustainable infrastructure management. Ultimately, this research provides not just a dataset for Aklavik, but a transferable and affordable methodological blueprint for empowering remote Arctic communities to actively monitor and mitigate the impacts of climate change on their vital infrastructure.

6. Conclusions

This study successfully demonstrated the capability of a very low-cost, consumer-grade UAV combined with Structure-

from-Motion photogrammetry for high-resolution snow depth mapping and insulation pattern derivation in the Arctic community of Aklavik, NT. Our methodology produced a detailed snow depth map revealing substantial spatial variability across the landscape. Key methodological findings confirmed the high accuracy of the dataset's alignment over stable, bare surfaces, indicated by a small median offset of +8.24 cm on snow-cleared roads. The results also characterized the primary challenge of this method: a systematic underestimation of snow depth in areas with shrubs, which occurs because the photogrammetric process captures the top of the vegetation canopy in the snow-free reference survey.

Crucially, this research translated these physical snow measurements into their direct thermal consequences for the underlying permafrost. By calculating the snow-induced surface temperature bias (ΔT_s), we quantified the substantial warming effect snow exerts on the ground, with localized insulation creating effects of up to 6.59 °C. The findings revealed that infrastructure and associated snow management create distinct thermal "hotspots". Snow accumulation was found to be deeper and its insulating effect more pronounced adjacent to roads compared to buildings, leading to a greater warming of the ground along transportation corridors.

This additional warming is a critical threat in a landscape where ambient air temperatures are already close to the threshold for permafrost instability. The fact that over 45% of road segments and nearly 35% of areas next to buildings experience a mean warming bias greater than 2.0 °C highlights a widespread, existing risk. Ultimately, this work provides not just a dataset for Aklavik, but a transferable and affordable methodological blueprint for empowering remote Arctic communities to actively identify, monitor, and mitigate these localized thermal hazards to their vital infrastructure.

Acknowledgements

The UndercoverEisAgenten project was funded by the Federal Ministry of Research, Technology and Space (German: Bundesministerium Forschung, Technologie und Raumfahrt, BMFTR) under the funding code 01BF2115A of the second Citizen Science funding guideline (2021–2024) (German: zweite Förderrichtlinie Citizen Science (2021–2024)). We would like to thank the volunteers of Moose Kerr School in Aklavik as well as the general community of Aklavik participating in UAV image acquisition campaigns and in mapping sessions as a part of the project. ML acknowledges funding from the European Union's HORIZON Europe program under Grant Agreement No. 101133587 (ILLUQ). During the preparation of this work, the authors used Google Gemini 2.5 and 3 Pro in order to improve the readability and language of the manuscript. After using this tool/service, the authors reviewed and edited the content as needed and take full responsibility for the content of the published article.

Article information

History dates

Received: 21 August 2025
Accepted: 2 February 2026
Accepted manuscript online: 12 February 2026
Version of record online: 1 April 2026

Data availability

Python scripts for data processing and analysis as described in Section 3 are available at https://gitlab.com/dlr-dw/uav-snow-depth-monitoring/. The high-resolution UAV orthomosaic and DSM datasets for Aklavik from September 2022 and March 2024, which were generated and analyzed for this study, are openly available in the Zenodo repository (https://doi.org/10.5281/zenodo.14608566) and can be cited as Mueller et al. (2025).

Author information

Author ORCIDs

Marlin M. Mueller https://orcid.org/0000-0001-7267-3886
Steffen Dietenberger https://orcid.org/0009-0003-2771-6068
Clémence Dubois https://orcid.org/0009-0003-0542-0514
Soraya Kaiser https://orcid.org/0000-0001-8179-5084
Pauline Walz https://orcid.org/0009-0002-3764-8567
Josefine Lenz https://orcid.org/0000-0002-4050-3169
Oliver Fritz https://orcid.org/0000-0001-6324-7295
Christian Thiel https://orcid.org/0000-0001-5144-8145
Moritz Langer https://orcid.org/0000-0002-2704-3655

Author contributions

Conceptualization: MM, ML
Data curation: MM, SK, JL, OF, CT, ML
Formal analysis: MM, ML
Funding acquisition: CT, ML
Investigation: MM, ML
Methodology: MM, CD, ML
Project administration: SK, JL, CT, ML
Resources: MM, SK, PW, JL, OF, SM, CT
Software: MM, SD, ML
Supervision: CD, CT, ML
Validation: MM, SD, ML
Visualization: MM
Writing – original draft: MM
Writing – review & editing: MM, SD, CD, SK, PW, JL, OF, SM, CT, ML

Competing interests

The authors declare that they have no known competing financial interests or personal relationships that could have appeared to influence the work reported in this paper.

Community involvement

This research was conducted as a community-engaged project in Aklavik, NT, in partnership with the Moose Kerr School and community members through the "UndercoverEisAgen-

ten" project. Community partners, including students, were actively involved in the data collection process through participation in UAV image acquisition campaigns and mapping sessions. This collaborative approach was crucial for enabling frequent and timely data gathering. The outcomes of this study, including detailed maps of hazardous snow accumulation, directly benefit the community by providing a cost-effective tool to monitor and mitigate risks to vital infrastructure from permafrost thaw, thereby contributing to local climate adaptation strategies.

References

Aga, J., Willmes, C., Sinitsyn, A.O., Arlov, T.B., Boike, J., and Westermann, S. 2025. Impact of snow and building management on ground surface temperatures in permafrost environments: a case study from the historical mining town ny-Ålesund, svalbard. Cold Regions Science and Technology, **237**: 104516. doi:10.1016/j.coldregions.2025.104516.

Batenipour, H., Kurz, D., Alfaro, M., Graham, J., and Ng, T.N.S. 2012. Highway embankment on degrading permafrost. *In* Cold Regions Engineering 2009: Proceedings. pp. 512–521. doi:10.1061/41072(359)50.

Bernard, E., Friedt, J.M., and Griselin, M. 2021. Snowcover survey over an arctic glacier forefield: contribution of photogrammetry to identify "icing" variability and processes. Remote Sensing, **13**(10). doi:10.3390/rs13101978.

Berra, E.F., and Peppa, M.V. 2020. Advances and challenges of uav sfm mvs photogrammetry and remote sensing: short review. In 2020 IEEE Latin American GRSS & ISPRS Remote Sensing Conference (LAGIRS). pp. 533–538. doi:10.1109/LAGIRS48042.2020.9285975.

Brown, R., and Brasnett, B. 2010. Canadian Meteorological Centre (CMC) daily snow depth analysis data, version 1. doi:10.5067/W9FOYWH0EQZ3.

Bühler, Y., Marty, M., Egli, L., Veitinger, J., Jonas, T., Thee, P., and Ginzler, C. 2015. Snow depth mapping in high-alpine catchments using digital photogrammetry. The Cryosphere, **9**(1): 229–243. doi:10.5194/tc-9-229-2015.

Bührle, L.J., Marty, M., Eberhard, L.A., Stoffel, A., Hafner, E.D., and Bühler, Y. 2023. Spatially continuous snow depth mapping by aeroplane photogrammetry for annual peak of winter from 2017 to 2021 in open areas. The Cryosphere, **17**(8): 3383–3408. doi:10.5194/tc-17-3383-2023.

Burn, C.R., and Kokelj, S.V. 2009. The environment and permafrost of the Mackenzie Delta Area. Permafrost and Periglacial Processes, **20**(2): 83–105. doi:10.1002/ppp.655.

Callaghan, T.V., Johansson, M., Brown, R.D., Groisman, P.Y., Labba, N., Radionov, V., et al. 2012. The changing face of Arctic snow cover: a synthesis of observed and projected changes. AMBIO, **40**(1): 17–31.

Canada, S. 2023. Provinces and territories cartographic boundary file. Available from https://www12.statcan.gc.ca/census-recensement/2021/geo/sip-pis/boundary-limites/index2021-eng.cfm?year=21 [accessed May 2025].

Cao, B., Wang, S., Hao, J., Sun, W., and Zhang, K. 2023. Inconsistency and correction of manually observed ground surface temperatures over snow-covered regions. Agricultural and Forest Meteorology, **338**: 109518. doi:10.1016/j.agrformet.2023.109518.

Chen, N., Wang, X., Yuan, F., Song, Y., Sun, L., Zuo, Y., et al. 2025. Warming-independent shortened snow cover duration enhances vegetation greening across northern permafrost region. Communications Earth & Environment, **6**(1): 250. doi:10.1038/s43247-025-02211-6.

Chen, R., von Deimling, T.S., Boike, J., Wu, Q., and Langer, M. 2023. Simulating the thermal regime of a railway embankment structure on the tibetan plateau under climate change. Cold Regions Science and Technology, **212**: 103881. doi:10.1016/j.coldregions.2023.103881.

Chen, Y. 2023. Spatial autocorrelation equation based on Moran's index. Scientific Reports, **13**(1): 19296. doi:10.1038/s41598-023-45947-x.

Cimoli, E., Marcer, M., Vandecrux, B., Bøggild, C.E., Williams, G., and Simonsen, S.B. 2017. Application of low-cost uass and digital photogrammetry for high-resolution snow depth mapping in the arctic. Remote Sensing, **9**(11). doi:10.3390/rs9111144.

Clark, A., Moorman, B.J., and and, D.W. 2023. UAV-SfM and geographic object-based image analysis for measuring multi-temporal planimetric and volumetric erosion of arctic coasts. Canadian Journal of Remote Sensing, **49**(1): 2211679. doi:10.1080/07038992.2023.2211679.

Clark, D.G., Ford, J.D., and Tabish, T. 2018. What role can unmanned aerial vehicles play in emergency response in the arctic: a case study from Canada. PLoS One, **13**(12):1–16. doi:10.1371/journal.pone.0205299.

Damseaux, A., Matthes, H., Dutch, V.R., Wake, L., and Rutter, N. 2025. Impact of snow thermal conductivity schemes on pan-Arctic permafrost dynamics in the community land model version 5.0. The Cryosphere, **19**(4): 1539–1558. doi:10.5194/tc-19-1539-2025.

Deems, J.S., Painter, T.H., and Finnegan, D.C. 2013. Lidar measurement of snow depth: a review. Journal of Glaciology, **59**(215): 467–479. doi:10.3189/2013JoG12J154.

Derksen, C., and Mudryk, L. 2023. Assessment of arctic seasonal snow cover rates of change. The Cryosphere, **17**(4): 1431–1443. doi:10.5194/tc-17-1431-2023.

DJI 2021. DJI Mini 2 User Manual. DJI. Available from https://dl.djicdn.com/downloads/DJI_Mini_2/20210630/DJI_Mini_2_User_Manual-EN.pdf [accessed 21 May 2025].

Dobinski, W. 2011. Permafrost. Earth-Science Reviews, **108**(3): 158–169. doi:10.1016/j.earscirev.2011.06.007.

Douglas, D.H., and Peucker, T.K. 1973. Algorithms for the reduction of the number of points required to represent a digitized line or its caricature. Cartographica, **10**(2): 112–122. doi:10.3138/FM57-6770-U75U-7727.

Dutch, V.R., Rutter, N., Wake, L., Sandells, M., Derksen, C., Walker, B., et al. 2022. Impact of measured and simulated tundra snowpack properties on heat transfer. The Cryosphere, **16**(10): 4201–4222. doi:10.5194/tc-16-4201-2022.

Eker, R., Bühler, Y., Schlögl, S., Stoffel, A., and Aydın, A. 2019. Monitoring of snow cover ablation using very high spatial resolution remote sensing datasets. Remote Sensing, **11**(6). doi:10.3390/rs11060699.

Fraser, R.H., Olthof, I., Lantz, T.C., and Schmitt, C. 2016. UAV photogrammetry for mapping vegetation in the low-arctic. Arctic Science, **2**(3): 79–102. doi:10.1139/as-2016-0008.

Fritz, O., Marx, S., Herfort, B., Kaiser, S., Langer, M., Lenz, J., et al. 2022. Das potenzial von citizen science für die kartierung von landschaftsveränderungen in arktischen permafrostregionen. AGIT: Journal für Angewandte Geoinformatik, **8**: 30–40. doi:10.14627/537728004.

Gabrlik, P., Janata, P., Zalud, L., and Harcarik, J. 2019. Towards automatic UAS-based snow-field monitoring for microclimate research. Sensors, **19**(8). doi:10.3390/s19081945.

Gaffey, C., and Bhardwaj, A. 2020. Applications of unmanned aerial vehicles in cryosphere: latest advances and prospects. Remote Sensing, **12**(6). doi:10.3390/rs12060948.

Gill, H.K., Lantz, T.C., Neill, B., and Kokelj, S.V. 2014. Cumulative impacts and feedbacks of a gravel road on shrub tundra ecosystems in the peel plateau, northwest territories, Canada. Arctic, Antarctic, and Alpine Research, **46**(4): 947–961. doi:10.1657/1938-4246-46.4.947.

Gisnås, K., Westermann, S., Schuler, T.V., Melvold, K., and Etzelmüller, B. 2016. Small-scale variation of snow in a regional permafrost model. The Cryosphere, **10**(3): 1201–1215. doi:10.5194/tc-10-1201-2016.

Gleason, S., Lim, J., Church, L.M., Jones, W., Nicolai, C., Pleasant, J., et al. 2023. Nalaquq ("it is found"): a knowledge co-production framework for environmental sensing and communication in indigenous arctic communities. Journal of Computer-Mediated Communication, **28**(5): zmad030. doi:10.1093/jcmc/zmad030.

Google 2025. Map of Aklavik, NWT, Canada. Available from https://www.google.com/maps/place/Aklavik [accessed 8 May 2025].

Government of Canada 2024. Monthly data report for: AKLAVIK A. Web Page. Available from https://climate.weather.gc.ca/historical_data/search_historic_data_e.html [accessed 2 June 2025]. Climate ID: 2200100; Latitude: 68.22; Longitude: -135.01; Elevation: 6.40 m; Page Modified: 2024-10-01.

Government of Northwest Territories 2024. Winter roads average open/close dates. Web Page. Available from https://www.inf.gov.nt.ca/en/services/highways-ferries-and-winter-roads/winter-roads-average-openclose-dates [accessed 2 June 2025]. Updated: June 3, 2024.

Hammar, J., Grünberg, I., Kokelj, S.V., van der Sluijs, J., and Boike, J. 2023. Snow accumulation, albedo and melt patterns following road construction on permafrost, Inuvik–Tuktoyaktuk Highway, Canada. The Cryosphere, **17**(12): 5357–5372. doi:10.5194/tc-17-5357-2023.

Harder, P., Pomeroy, J.W., and Helgason, W.D. 2020. Improving subcanopy snow depth mapping with unmanned aerial vehicles: lidar versus Structure-from-Motion techniques. The Cryosphere, **14**(6):1919–1935. doi:10.5194/tc-14-1919-2020.

Harris, S.A. 1986. Permafrost distribution, zonation and stability along the eastern ranges of the cordillera of north america. Arctic, **39**(1): 29–38.

Hinkel, K.M., and Hurd Jr, J.K. 2006. Permafrost destabilization and thermokarst following snow fence installation, Barrow, Alaska, USA. Arctic, Antarctic, and Alpine Research, **38**(4):530–539. doi:10.1657/1523-0430(2006)38[530:PDATFS]2.0.CO;2.

Hjort, J., Streletskiy, D., Doré, G., Wu, Q., Bjella, K., and Luoto, M. 2022. Impacts of permafrost degradation on infrastructure. Nature Reviews Earth & Environment, **3**(1): 24–38. doi:10.1038/s43017-021-00247-8.

Hopkinson, C., Sitar, M., Chasmer, L., and Treitz, P. 2004. Mapping snowpack depth beneath forest canopies using airborne lidar. Photogrammetric Engineering and Remote Sensing, **70**(3):323–330. doi:10.14358/PERS.70.3.323.

Jacobs, J.M., Hunsaker, A.G., Sullivan, F.B., Palace, M., Burakowski, E.A., Herrick, C., and Cho, E. 2021. Snow depth mapping with unpiloted aerial system lidar observations: a case study in durham, new hampshire, united states. The Cryosphere, **15**(3): 1485–1500. doi:10.5194/tc-15-1485-2021.

James, M.R., and Robson, S. 2014. Mitigating systematic error in topographic models derived from uav and ground-based image networks. Earth Surface Processes and Landforms, **39**(10): 1413–1420. doi:10.1002/esp.3609.

James, M.R., Chandler, J.H., Eltner, A., Fraser, C., Miller, P.E., Mills, J.P., et al. 2019. Guidelines on the use of Structure-from-Motion photogrammetry in geomorphic research. Earth Surface Processes and Landforms, **44**(10): 2081–2084. doi:10.1002/esp.4637.

Jiang, S., Jiang, W., and Wang, L. 2022. Unmanned aerial vehicle-based photogrammetric 3D mapping: a survey of techniques, applications, and challenges. IEEE Geoscience and Remote Sensing Magazine, **10**(2): 135–171. doi:10.1109/MGRS.2021.3122248.

Johansson, M., Callaghan, T.V., kerman, H.J., Jackowicz-Korczynski, M., and Christensen, T.R. 2013. Rapid responses of permafrost and vegetation to experimentally increased snow cover in sub-arctic sweden. Environmental Research Letters, **8**(3): 035025. doi:10.1088/1748-9326/8/3/035025.

Kaiser, S., Boike, J., Grosse, G., and Langer, M. 2022. The potential of UAV imagery for the detection of rapid permafrost degradation: assessing the impacts on critical arctic infrastructure. Remote Sensing, **14**(23). doi:10.3390/rs14236107.

Kaiser, S., Boike, J., Grosse, G., and Langer, M. 2024. Multisource synthesized inventory of CRitical Infrastructure and HUman-Impacted Areas in AlaSka (SIRIUS). Earth System Science Data, **16**(8): 3719–3753. doi:10.5194/essd-16-3719-2024.

Khani, H.M., Kinnard, C., and Lévesque, E. 2022. Historical trends and projections of snow cover over the high arctic: a review. Water, **14**(4). doi:10.3390/w14040587.

Klock, R., Hudson, E., Aihoshi, D., and Mullock, J. 2001. The Weather of the Yukon, Northwest Territories and Western Nunavut: Graphic Area Forecast 35. NAV CANADA, Ottawa, ON. Available from https://www.navcanada.ca/en/lawm-yukon-nwt-en.pdf [accessed June 2025].

Lamare, M., Domine, F., Revuelto, J., Pelletier, M., Arnaud, L., and Picard, G. 2023. Investigating the role of shrub height and topography in snow accumulation on low-arctic tundra using UAV-borne lidar. Journal of Hydrometeorology, **24**(5): 853–871. doi:10.1175/JHM-D-22-0067.1.

Landers, K., and Streletskiy, D. 2023. (Un)frozen foundations: a study of permafrost construction practices in Russia, Alaska, and Canada. Ambio, **52**(7): 1170–1183. doi:10.1007/s13280-023-01866-9.

Langer, M., Schneider von Deimling, T., Westermann, S., Rolph, R., Rutte, R., Antonova, S., et al. 2023. Thawing permafrost poses environmental threat to thousands of sites with legacy industrial contamination. Nature Communications, **14**(1): 1721. doi:10.1038/s41467-023-37276-4.

Lendzioch, T., Langhammer, J., and Jenicek, M. 2019. Estimating snow depth and leaf area index based on uav digital photogrammetry. Sensors, **19**(5). doi:10.3390/s19051027.

Li, Y., Zhu, L., Gong, P., and H.S. 2010. A refined marker controlled watershed for building extraction from dsm and imagery. International Journal of Remote Sensing, **31**(6): 1441–1452. doi:10.1080/01431160903475373.

Lim, J.S., Gleason, S., Williams, M., Linares, Matás G.J., Marsden, D., and Jones, W. 2022. UAV-based remote sensing for managing alaskan native heritage landscapes in the Yukon-Kuskokwim Delta. Remote Sensing, **14**(3). doi:10.3390/rs14030728.

Ling, F., and Zhang, T. 2003. Impact of the timing and duration of seasonal snow cover on the active layer and permafrost in the Alaskan Arctic. Permafrost and Periglacial Processes, **14**(2): 141–150. doi:10.1002/ppp.445.

Litchi 2023. Litchi website. Available from https://flylitchi.com/ [accessed 7 May 2025].

Luojus, K., Pulliainen, J., Takala, M., Lemmetyinen, J., Mortimer, C., Derksen, C., et al. 2021. GlobSnow v3.0 Northern Hemisphere snow water equivalent dataset. doi:10.1038/s41597-021-00939-2.

Maier, K., Nascetti, A., van Pelt, W., and Rosqvist, G. 2022. Direct photogrammetry with multispectral imagery for uav-based snow depth estimation. ISPRS Journal of Photogrammetry and Remote Sensing, **186**: 1–18. doi:10.1016/j.isprsjprs.2022.01.020.

Mamun, A.A., and Natcher, D.C. 2023. The promise and pitfalls of community-based monitoring with a focus on canadian examples. Environmental Monitoring and Assessment, **195**(4): 445. doi:10.1007/s10661-022-10841-y.

Manos, E., Witharana, C., and Liljedahl, A.K. 2025. Permafrost thaw-related infrastructure damage costs in Alaska are projected to double under medium and high emission scenarios. Communications Earth & Environment, **6**(1): 221. doi:10.1038/s43247-025-02191-7.

Masný, M., Weis, K., and Biskupič, M. 2021. Application of fixed-wing UAV-based photogrammetry data for snow depth mapping in alpine conditions. Drones, **5**(4). doi:10.3390/drones5040114.

Meier, W., Markus, T., and Comiso, J. 2018. AMSR-E/AMSR2 unified L3 daily 12.5 km brightness temperatures, sea ice concentration, motion; snow depth polar grids, version 1. Available from http://nsidc.org/data/AU_SI12/versions/1. doi:10.5067/RA1MIJOYPK3P.

Mellor, M. 1977. Engineering properties of snow. Journal of Glaciology, **19**(81): 15–66. doi:10.3189/S002214300002921X.

Meriö, L.J., Rauhala, A., Ala-aho, P., Kuzmin, A., Korpelainen, P., Kumpula, T., et al. 2023. Measuring the spatiotemporal variability in snow depth in subarctic environments using uass – part 2: snow processes and snow–canopy interactions. The Cryosphere, **17**(10): 4363–4380. doi:10.5194/tc-17-4363-2023.

Microsoft 2025. Map of Aklavik, NWT, Canada. Bing Maps. Available from https://www.bing.com/maps?ty=30&q=Aklavik [accessed 8 May 2025].

Mohammadzadeh Khani, H., Kinnard, C., and Lévesque, E. 2022. Historical trends and projections of snow cover over the high arctic: a review. Water, **14**(4). doi:10.3390/w14040587.

Mueller, M.M., Dietenberger, S., Nestler, M., Dubois, C., Kaiser, S., Lenz, J., et al. 2024. Undercovereisagenten - integrating low-cost uavs and community insights for enhanced permafrost monitoring. In IGARSS 2024-2024 IEEE International Geoscience and Remote Sensing Symposium. pp. 3893–3896. doi:10.1109/IGARSS53475.2024.10642540.

Mueller, M.M., Dietenberger, S., Nestler, M., Hese, S., Ziemer, J., Bachmann, F., et al. 2023. Novel UAV flight designs for accuracy optimization of structure from motion data products. Remote Sensing, **15**(17). doi:10.3390/rs15174308.

Mueller, M.M., Thiel, C., Kaiser, S., Lenz, J., Langer, M., Fritz, O., and Marx, S. 2025. High-resolution UAV Orthomosaic and DSM Dataset – Aklavik, NWT, CA 10 cm GSD [2022, 2024]. doi:10.5281/zenodo.14608566.

Natural Resources Canada 2023. Permafrost Atlas of Canada. Map Service, The Atlas of Canada, 5th ed. Available from https://maps-cartes.services.geo.ca/server_serveur/rest/services/NRCan/permafrost_atlas_of_canada_en/MapServer [accessed 10 December 2025].

Neill, H.B., and Burn, C.R. 2017. Impacts of variations in snow cover on permafrost stability, including simulated snow management, Dempster Highway, Peel Plateau, Northwest Territories. Arctic Science, **3**(2): 150–178. doi:10.1139/as-2016-0036.

Nitzbon, J., Schneider von Deimling, T., Aliyeva, M., Chadburn, S.E., Grosse, G., Laboor, S., et al. 2024. No respite from permafrost-thaw impacts in the absence of a global tipping point. Nature Climate Change, **14**(6): 573–585. doi:10.1038/s41558-024-02011-4.

Nota, E., Nijland, W., and de Haas, T. 2022. Improving UAV-SfM time-series accuracy by co-alignment and contributions of ground control or RTK positioning. International Journal of Applied Earth Observation and Geoinformation, **109**: 102772. doi:10.1016/j.jag.2022.102772.

NWT Bureau of Statistics 2024. Population estimates by community. Web Page. Available from https://www.statsnwt.ca/population/population-estimates/bycommunity.php [accessed 2 June 2025].

Oldroyd, H., Higgins, C., Huwald, H., Selker, J., and Parlange, M. 2013. Thermal diffusivity of seasonal snow determined from temperature profiles. Advances in Water Resources, **55**: 121–130. doi:10.1016/j.advwatres.2012.06.011

OpenStreetMap contributors. 2025. Planet dump. Available from https://planet.osm.org, https://www.openstreetmap.org [accessed June 2025].

Park, H., Fedorov, A.N., Zheleznyak, M.N., Konstantinov, P.Y., and Walsh, J.E. 2015. Effect of snow cover on pan-arctic permafrost thermal regimes. Climate Dynamics, **44**(9): 2873–2895. doi:10.1007/s00382-014-2356-5.

Pedersen, C., Otokiak, M., Koonoo, I., Milton, J., Maktar, E., Anaviapik, A., et al. 2020. Sciq: an invitation and recommendations to combine science and inuit qaujimajatuqangit for meaningful engagement of inuit communities in research. Arctic Science, **6**(3): 326–339. doi:10.1139/as-2020-0015.

Peng, X., Frauenfeld, O.W., Huang, Y., Chen, G., Wei, G., Li, X., et al. 2024. The thermal effect of snow cover on ground surface temperature in the Northern Hemisphere. Environmental Research Letters, **19**(4): 044015. doi:10.1088/1748-9326/ad30a5.

Pina, P., and Vieira, G. 2022. UAVs for science in Antarctica. Remote Sensing, **14**(7). doi:10.3390/rs14071610.

Porter, C., Howat, I., Noh, M.J., Husby, E., Khuvis, S., Danish, E., et al. 2022. ArcticDEM – Strips, Version 4.1. doi:10.7910/DVN/C98DVS.

Prokop, A., Schirmer, M., Rub, M., Lehning, M., and Stocker, M. 2008. A comparison of measurement methods: terrestrial laser scanning, tachymetry and snow probing for the determination of the spatial snow-depth distribution on slopes. Annals of Glaciology, **49**: 210–216. doi:10.3189/172756408787814726.

Qingbai, W., Yuanlin, Z., and Yonzhi, L. 2002. Evaluation model of permafrost thermal stability and thawing sensibility under engineering activity. Cold Regions Science and Technology, **34**(1): 19–30. doi:10.1016/S0165-232X(01)00047-7.

Rantanen, M., Karpechko, A.Y., Lipponen, A., Nordling, K., rinen, O., Ruosteenoja, K., et al. 2022. The arctic has warmed nearly four times faster than the globe since 1979. Communications Earth & Environment, **3**(1): 168. doi:10.1038/s43247-022-00498-3.

Rettelbach, T., Nitze, I., Grünberg, I., Hammar, J., Schäffler, S., Hein, D., et al. 2024. Very high resolution aerial image orthomosaics, point clouds, and elevation datasets of select permafrost landscapes in Alaska and Northwestern Canada. Earth System Science Data, **16**(12): 5767–5798. doi:10.5194/essd-16-5767-2024.

Revuelto, J., Alonso-Gonzalez, E., Vidaller-Gayan, I., Lacroix, E., Izagirre, E., pez, G., and pez-Moreno, J.I. 2021. Intercomparison of UAV platforms for mapping snow depth distribution in complex alpine terrain. Cold Regions Science and Technology, **190**: 103344. doi:10.1016/j.coldregions.2021.103344.

Schneider von Deimling, T., Lee, H., Ingeman-Nielsen, T., Westermann, S., Romanovsky, V., Lamoureux, S., et al. 2021. Consequences of permafrost degradation for arctic infrastructure—bridging the model gap between regional and engineering scales. The Cryosphere, **15**(5): 2451–2471. doi:10.5194/tc-15-2451-2021.

Slater, A.G., Lawrence, D.M., and Koven, C.D. 2017. Process-level model evaluation: a snow and heat transfer metric. The Cryosphere, **11**(2): 989–996. doi:10.5194/tc-11-989-2017.

Stieglitz, M., Déry, S.J., Romanovsky, V.E., and Osterkamp, T.E. 2003. The role of snow cover in the warming of arctic permafrost. Geophysical Research Letters, **30**(13). doi:10.1029/2003GL017337.

Streletskiy, D.A., Clemens, S., Lanckman, J.P., and Shiklomanov, N.I. 2023. The costs of arctic infrastructure damages due to permafrost degradation. Environmental Research Letters, **18**(1): 015006. doi:10.1088/1748-9326/acab18.

Sturm, M., Holmgren, J., König, M., and Morris, K. 1997. The thermal conductivity of seasonal snow. Journal of Glaciology, **43**(143): 26–41. doi:10.3189/S0022143000002781.

Swaszek, P.F., Hartnett, R.J., Seals, K.C., Siciliano, J.D., and Swaszek, R.M.A. 2018. Limits on GNSS performance at high latitudes. *In* Proceedings of the 2018 International Technical Meeting of The Institute of Navigation. The Institute of Navigation, Reston, Virginia. pp. 160–176. doi:10.33012/2018.15549.

Tanguy, R., Bartsch, A., Nitze, I., Irrgang, A., Petzold, P., Widhalm, B., et al. 2024. Pan-Arctic assessment of coastal settlements and infrastructure vulnerable to coastal erosion, sea-level rise, and permafrost thaw. Earth's Future, **12**(12): e2024EF005013. doi:10.1029/2024EF005013. E2024EF005013 2024EF005013.

Van der Sluijs, J., Kokelj, S.V., Fraser, R.H., Tunnicliffe, J., and Lacelle, D. 2018. Permafrost terrain dynamics and infrastructure impacts revealed by UAV photogrammetry and thermal imaging. Remote Sensing, **10**(11). doi:10.3390/rs10111734.

Vander Jagt, B., Lucieer, A., Wallace, L., Turner, D., and Durand, M. 2015. Snow depth retrieval with uas using photogrammetric techniques. Geosciences, **5**(3): 264–285. doi:10.3390/geosciences5030264.

Vergnano, A., Franco, D., and Godio, A. 2022. Drone-borne ground-penetrating radar for snow cover mapping. Remote Sensing, **14**(7). doi:10.3390/rs14071763.

Walker, B., Wilcox, E.J., and Marsh, P. 2020. Accuracy assessment of late winter snow depth mapping for tundra environments using Structure-from-Motion photogrammetry. Arctic Science, **7**(3): 588–604. doi:10.1139/as-2020-0006.

Walz, P., Fritz, O., Marx, S., Mueller, M.M., Thiel, C., Lenz, J., et al. 2025. Monitoring arctic permafrost—examining the contribution of volunteered geographic information to mapping ice-wedge polygons. The Cryosphere, **19**(12): 6355–6379. doi:10.5194/tc-19-6355-2025.

Wilson, N.J., Worden, E., and O'Hanlon, G. 2024. Connecting community-based monitoring to arctic environmental decision-making and governance: a systematic scoping review of the literature. Arctic Science, **10**(2): 261–280. doi:10.1139/as-2023-0034.

Zhang, C., Douglas, T.A., and Anderson, J.E. 2021. Modeling and mapping permafrost active layer thickness using field measurements and remote sensing techniques. International Journal of Applied Earth Observation and Geoinformation, **102**: 102455. doi:10.1016/j.jag.2021.102455.

Zhang, C., Douglas, T.A., Brodylo, D., Bosche, L.V., and Jorgenson, M.T. 2024. Combining a climate-permafrost model with fine resolution remote sensor products to quantify active-layer thickness at local scales. Environmental Research Letters, **19**(4): 044030. doi:10.1088/1748-9326/ad31dc.

Zhao, H., Li, G., Chen, Z., Zhang, S., Zhang, B., and Cheng, X. 2024. Impacts of GCP distributions on UAV-PPK photogrammetry at Sermeq Avannarleq Glacier, Greenland. Remote Sensing, **16**(21). doi:10.3390/rs16213934.

Zhao, W., Mu, C., Wu, X., Zhong, X., Peng, X., Liu, Y., et al. 2023. Spatiotemporal characteristics and differences in snow density between the tibet plateau and the arctic. Remote Sensing, **15**(16). doi:10.3390/rs15163976.

Zinßer, T., Schmidt, J., and Niemann, H. 2005. Point set registration with integrated scale estimation. *In* International Conference on Pattern Recognition and Image Processing. pp. 116–119.

Appendix A. Detailed processing parameters

This appendix details the specific parameters used for various data processing steps described in the main text.

A1. Agisoft metashape processing parameters

For the SfM processing in Agisoft Metashape (versions 1.8.4 and 2.1.3), key parameters were set as follows:

- Image alignment accuracy: “Highest”
- Key point limit: 80 000
- Tie point limit: 8000
- Dense cloud generation quality: “High”
- Depth filtering mode: “Mild”

A2. CloudCompare ICP alignment parameters

For the fine registration of the September 2022 (reference) and March 2024 (data to be aligned) point clouds using the ICP algorithm implemented in CloudCompare (version 2.13.2 “Kharkiv”), the following parameters were utilized:

- RMS difference threshold for convergence: 1.0×10^{-7}
- Final Overlap (expected percentage of overlap between clouds): 90%
- Adjust scale: enabled
- Random sampling limit: 500 000 points (to balance computational efficiency with data representativeness)
- Farthest point removal: enabled (to mitigate the influence of outliers)
- Scalar field weights: applied to both reference (2022) and data (2024) clouds, using available scalar field information to guide registration.
- Constraints on transformation: no constraints were placed on rotation or translation.

A3. Orfeo ToolBox watershed segmentation parameters (building extraction)

For the semi-automated extraction of building footprints from the March 2024 DSM using the Orfeo ToolBox (OTB, version 8.1.2) within QGIS, the watershed segmentation algorithm was configured with the following parameters:

- Algorithm: “watershed”
- Depth Threshold: 0.01 (to increase sensitivity to subtle elevation changes indicative of building edges)
- Flood level: 0.1 (to control the merging of initial segmentation regions)
- Processing mode: “vector”
- Tile size: 4096 pixels (to balance memory usage and processing efficiency)
- Polygon stitching: enabled (to merge polygons representing the same object across tile boundaries)
- Minimum object size: 1000 pixels (to prevent the creation of numerous small, nonbuilding polygons)

Appendix B. Directional analysis of snow distribution on road embankments

To investigate the influence of prevailing winds on snow accumulation around infrastructure, a directional analysis was performed on the road buffer zones. Road embankments were segmented into four cardinal sectors (North, South, East, and West) based on their orientation relative to the road centerline.

Figure B1 presents the statistical distribution of mean and median snow depths for each sector. A Mann–Whitney *U* test with Bonferroni correction confirmed that South-facing embankments accumulate significantly deeper snow than those facing other directions. This asymmetry is consistent with leeward drift deposition driven by the prevailing Northwest winds observed in the region (Klock et al. 2001).

Fig. B1. Boxplots showing the distribution of mean and median snow depths around road embankments categorized by cardinal direction. “S” (South) represents buffers on the leeward side of the road relative to the prevailing Northwest winds, exhibiting significantly higher snow accumulation.

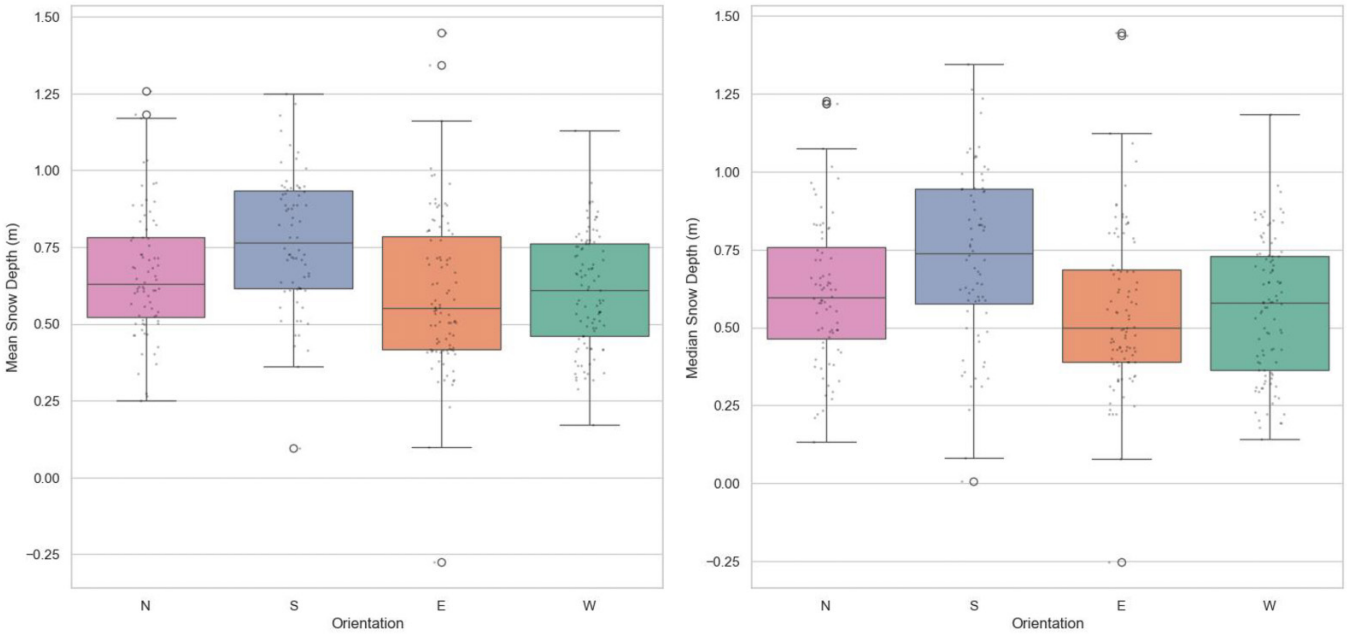

Appendix C. Derivation of potential snow insulation

This appendix details the steady-state model used to quantify the potential insulating effect of the snowpack, specifically its capacity to dampen the winter air temperature signal at the ground surface.

C1. Snow damping factor and temperature offset

The snow damping factor (n_f), ranging from 0 (perfect insulation) to 1 (no insulation), is calculated following Slater et al. (2017) as

$$n_f \approx e^{-S_{eff}/D} \quad \text{(C1)}$$

where S_{eff} is the effective snow depth and D is the damping depth defined as

$$D = \sqrt{\frac{2\kappa}{\omega}} \quad \text{(C2)}$$

where κ is the bulk thermal diffusivity of the snow cover and ω is the angular frequency of the freezing period.

Using this damping factor, the potential bias induced by the snow cover on the mean annual surface temperature (ΔT_s) is calculated as

$$\Delta T_s = \frac{FDD_a - FDD_s}{N_f + N_t} \quad \text{(C3)}$$

where N_t is the number of thawing days and FDD_a are the freezing degree days derived from near-surface air temperature T_{air}. FDD_s are the freezing degree days at the ground surface below the snow cover, calculated as

$$FDD_s = n_f FDD_a \quad \text{(C4)}$$

C2. Effective snow depth scaling

The effective snow depth (S_{eff}) is estimated by multiplying the UAV-derived snow depth (h_s, assumed to represent maximum depth) by a dimensionless scaling factor α:

$$S_{eff} \approx h_s \cdot \alpha \quad \text{(C5)}$$

The scaling factor α accounts for the typical seasonal evolution (accumulation and persistence). It is derived as the mean value from historical daily snow depth data (2010–2020) for Aklavik (Brown and Brasnett 2010). For each historical year, α is calculated as

$$\alpha = \left(\frac{\sum_{i=1}^{N_f} S_i \left(N_f + 1 - i\right)}{\sum_{i=1}^{N_f} i} \right) \quad \text{(C6)}$$

where S_i represents the daily snow depth normalized by the maximum snow depth within that year, N_f denotes the total number of snow-covered days, and i indexes each day. This integration ensures the factor reflects the actual duration and magnitude of snow cover over the season. Based on this historical analysis, the mean value was calculated as $\alpha \approx 0.70$.

C3. Thermal parameters and conductivity equations

The thermal diffusivity (κ) required for eq. C2 is derived using the formula $\kappa = \frac{k_{eff}}{\rho c_p}$, assuming a specific heat capacity of ice $c_p \approx 2090\,\mathrm{J\,kg^{-1}K^{-1}}$ (Oldroyd et al. 2013).

To estimate effective thermal conductivity (k_{eff}), we utilized the empirical regressions from Sturm et al. (1997).

For pixels outside the infrastructure mask (soft snow, $\rho = 0.23\ \mathrm{g\,cm^{-3}}$), the logarithmic relationship for low-density snow was used (Sturm eq. C3):

$$k_{eff} = 10^{(2.650\rho - 1.652)} \quad (\text{for } \rho \leq 0.6\ \mathrm{g\,cm^{-3}}) \quad \text{(C7)}$$

For pixels within the infrastructure mask (compacted snow, $\rho = 0.45\ \mathrm{g\,cm^{-3}}$), the quadratic regression was used (Sturm eq. 4):

$$k_{eff} = 0.138 - 1.01\rho + 3.233\rho^2 \quad \text{(C8)}$$

This quadratic form is noted by Sturm et al. (1997) for its reasonable extrapolation capability to denser snow found in managed areas.